UNIVERSITETET
I OSLO

Master Thesis

Structural changes in graphite-based anodes of Li-ion batteries elucidated through operando XRD

Abilash Kanish Thiagarajan

Materials Science for Energy and Nanotechnology (MENA)
60 ECTS credits

Department of Chemistry
The faculty of Mathematics and Natural Science

Structural changes in graphite-based anodes of Li-ion batteries elucidated through operando XRD

Material Science for Energy and Nanotechnology

Abilash K. Thiagarajan

2023

Structural changes in graphite-based anodes of Li-ion batteries elucidated through operando XRD.

Abilash K. Thiagarajan

http://www.duo.uio.no

Printed at Reprosentralen, University of Oslo

Abstract

Lithium-ion batteries (LIBs) with graphite-based anodes dominate the battery market around the world and have been studied extensively for the past decades, but the structural changes during cycling are still not fully understood.

In this work, we used galvanostatic cycling (GC) to characterize the electrochemical performance of graphite samples in LIB. We also attempted to achieve stable capacities over hundreds of cycles to monitor the effect of long-term cycling on the mechanisms of graphite, with limited success. The fabricated coin cells experienced poor capacity retention across all graphite samples and some abnormal capacity increases that had not been observed previously. We noticed that electrolytes containing FEC made a noticeable change to the electrochemical performance as it resulted in irregular cycling, but also better capacity retention.

Operando X-ray diffraction is a powerful technique to understand structural changes. We looked at multiple graphite reflections, mainly 002, 100, 101, 102 and 004, and observed that the expansion of the structure is not only 2 dimensions but all 3 dimensions as the interlayer distance and graphene layers expands during lithiation. We also monitored this expansion of graphene layers with pair distribution function (PDF) as the three C-C distances in hexagonal carbon rings, 1.41 Å, 2.41 Å and 2.85 Å, changed lengths at different points during lithiation and delithiation.

We looked at diffraction peaks during lithiation and delithiation to study the mechanisms and observed that they were different. Lithiation showed solid solution like behavior indicating disordered intermediate phases, while delithiation showed two-phase transition indicating ordered structures.

In this work we have used *Operando* X-ray diffraction to show that the structural changes graphite undergoes during cycling, transition from graphite to LiC_6, is not specific to each graphite sample and the structural changes depend on the condition of the material. Pristine graphite samples transitioned fully to LiC_6 during cycling with C-rate of C/6, but only LiC_{12} when a higher C-rate of C/2 was used. Graphite electrodes cut from commercial pouch cells that had cycled many hundreds of electrochemical cycles were able to transition to LiC_6 during C/20, but only LiC_{12} during C/6, indicating an "ageing" mechanism.

Acknowledgements

The work in this master thesis was carried out at the Nanostructures and Functional Materials group (NAFUMA) at the Department of Chemistry, Faculty of Mathematics and Natural Sciences at the University of Oslo (UiO), from August 2021 to May 2023.

This work was achievable due to multiple people. I would first like to thank my supervisors Anders Brennhagen, David S. Wragg and my main supervisor Alexey Y. Koposov who in each of their own ways helped me complete this project. I would also like to thank "En broder" who helped keep the RECX instruments running and assisted me with XRD measurements.

I was able to overcome these two years due to the many members at NAFUMA. I want to especially thank Salah Bra Amedi, Andrew Pastusic, Amalie Skurtveit and Casper E. Skautvedt for many enjoyable conversations and moments.

Finally, I would like to thank my brother who has been my best friend since the beginning and my parents who came to this country that was completely unknown to them with limited knowledge and worked hard to provide me with all the opportunities they never had.

University of Oslo, May 2023

Abilash K. Thiagarajan

Abbreviations

CB	Carbon black
CMC	Carboxymethylcellulose
EMC	Ethyl methyl carbonate
ESRF	European Synchrotron Radiation Facility
EV	Electric vehicle
GIC	Graphite intercalated compound
LIG	Li intercalated graphite
MoZEES	Moblity Zero Emission Energy Systems
OCV	Open-circuit voltage
SBR	Styrene-Butadiene Rubber
SEI	Solid electrolyte interphase
SHE	Standard hydrogen electrode
SNBL	Swiss-Norwegian beamlines
SoC	State of charge
SoH	State of Health
VC	Vinylene carbonate
XRD	X-ray diffraction

Table of Contents

1. Introduction

In the past decade, major efforts have been put into minimizing CO_2 emissions by transitioning to renewable energy sources from fossil fuels to minimize and possibly reverse global warming. This transition requires better systems for energy storage systems, where batteries play an important role. Following this movement, major car manufacturers are transitioning from gasoline-powered engines to electric vehicles. As a result, the world needs a large quantity of rechargeable batteries on a short notice to supply these rapidly growing demands. The growing demand for batteries will eventually lead to a shortage raw material needed to produce the batteries [1]. Therefore, the availability of raw materials in Europe has become a primary concern for European battery production, especially as natural graphite is widely used in anodes for batteries and is currently on EU's list of critical raw materials [2].Recycling of batteries will therefore become a necessity in the future address the problem of critical materials. At the present moment the recycling of Li-ion batteries is at the very beginning, as recycling of used batteries is not cost-effective and, therefore, many batteries may end up in landfills [3]. Recycling could be viewed in different ways – from the recycling of elements to recycling of materials or components. However, for efficient recycling the degradation mechanism must be properly understood. Then we can find out at which stage the graphite has changed to the point that recycling becomes difficult. The present work aims to understand the chemical mechanism taking place during cycling and provide some new insight in the differences in cycling mechanism between pristine and cycled samples for one of the most common battery materials – graphite.

1.1 Objectives

The primary objective of this study was to optimize graphite in battery cells and monitor the structural changes graphite undergoes while being cycled in a battery. Our aim was to see how different samples of graphite, both natural and synthetic with varying domain sizes and surface treatments would differ from each other. We acquired a variety of samples from MoZEES (Moblity Zero Emission Energy Systems) partners. We decided to measure varying graphite samples in order determine whether the observed results were specific for a certain graphite sample or not. The work done in this thesis is part of a greater goal of eventually recycling graphite anodes. In order to recycle these graphite anodes, we need to know more about the structural changes graphite undergoes during cycling. During battery testing, we focused on the evolution of different graphite reflections by utilizing *operando* X-ray diffraction.

1.2 History

Since Volta's discovery of the battery concept, one of the biggest breakthroughs in the field was done in 1860, by Gaston Planté. He invented the first practical version of the rechargeable battery based on lead-acid chemistry[4]. Each cell in the lead-acid battery pack provided approximately 2 V. The lead acid-battery had advantages of being cheap in manufacturing, had good recharge efficiency and could be operated at relatively large range of temperatures making it suitable for practical use. However, the lead-acid was also plagued with multiple disadvantages such as relatively low cycle life combined with self-discharge, low energy density, sulfation causing irreversible battery damage and the toxicity of lead. The heavy weight of such batteries was essentially a road block for early electromobility at the beginning of the 20th century. Despite these shortcomings, the lead-acid battery was a dominating secondary battery technology for many years, and they are still used as starter batteries in modern cars. Over the 20th century, substantial research efforts were devoted to find alternative and new technologies that could replace the lead-acid battery. These studies gave rise to multiple battery chemistries, and chemistries involving alkali metals became the most appealing. By the 1970s, Li metal was already used as an anode material in primary (non-rechargeable) batteries due to its high theoretical specific capacity of 3 860 mAh/g and low redox potential at -3.04 V vs standard hydrogen electrode (SHE) [5]. In 1976, Whittingham demonstrated a revolutionary secondary (rechargeable) battery with TiS_2 as the cathode and Li metal as the anode to demonstrate the principle of a rechargeable intercalation battery. The cell utilized intercalation chemistry to create a high energy density reversible battery. This new battery chemistry had voltage close to 2.2 V and a specific capacity of 209 mAh/g for the cathode [6]. In 1980, shortly after Whittingham's experiments, Goodenough and his research group published their discovery of Li-ion intercalation in $LiCoO_2$ (LCO). LCO was found to be a better cathode material in Li-ion batteries (LIB) compared to TiS_2 as it exhibited high open-circuit voltages (OCV) in the range of 3.9-4.2 V vs Li/Li^+ and a theoretical capacity of 247 mAh/g [7]. However, further experimentation demonstrated that the use of Li metal as an anode material in LIBs is problematic. The cyclability and fire safety were the main problems to appear due to the formation of Li dendrites and lack of proper cell packaging technologies.

In 1983 Yazami showed that Li-ions could intercalate into graphite at a desirably low voltage, which essentially solved the safety concerns associated with the use of metallic Li as an anode. Graphite has an ideal layered structure where the van der Walls forces between the graphene sheets are weak so that, under certain conditions, different molecules, atoms or ions could penetrate into the host structure between the graphene layers. This leads to an increase the interlayer distance along the c-axis and forms a graphite intercalated compound (GIC). Demonstrated intercalation of Li-ion into the graphite structure provided an anode material with stable cycling performance and reasonable gravimetric capacity at 372 mAh g^{-1}. As a result, graphite was deployed as an anode material in LIBs with $LiCoO_2$ as a cathode [8], which was commercialized by SONY in 1991 [9]. That commercial effort demonstrated a great potential of the Li-ion battery technology for any mobile application. Relatively low mass and volume coupled with high energy density made Li-ion batteries enablers of the EV boom, which we witness today.

The work in this thesis is focused on understanding the anode materials for Li-ion batteries, therefore, anode materials will be the focal point of further review. While multiple chemical systems have been proposed as anode materials over the years (including Si, LTO,NTO), graphite still remains the dominant anode material for Li-ion batteries.

There are mainly two different types of graphite used in commercial LIBs produced and sold worldwide: natural and synthetic. As implied, natural graphite is mined and processed into a battery-grade product that can be used for cell production. Most of the worlds supply of natural graphite that can be used in LIBs is mainly distributed in a few countries i.e. China, Mexico, Czech and Brazil. That puts in question its worldwide supply in the upcoming years, and thus graphite appeared on EU’s list of critical raw materials due to geographically limited supply and increasing demand [2]. Natural graphite usually possesses anisotropic features, which restricts the random transportation and diffusion of Li-ions into the graphite structure during the intercalation/deintercalation process [10]. As a result, natural graphite often needs a series of complex modification processes such as spheroidization and amorphous carbon coating before being used as an anode in LIBs [10].

Synthetic graphite, created as an alternative to the natural graphite, is a manufactured product synthesized from a carbon precursor, (typically petroleum coke or needle coke) through a process called graphitization. The major drawback of synthetic graphite is the high temperature (2000-2800°C), process required for graphitization, which in return increases carbon footprint of LIBs utilizing synthetic graphite. Additionally, only the graphite prepared at 2800°C has a perfect layered structure with high graphitization degree and relatively large surface area with well-developed mesopores (pores with diameter between 2-50 nm), which offers a favorable pathway for the electrochemical intercalation/deintercalation of Li-ions in the carbon matrix [11].

2. Theory and previous works

2.1 The working principles of LIBs

A basic Li-ion battery cell consists of a cathode and an anode with electrolyte containing Li-ions filling the space between the electrodes. These electrodes are also isolated from each other by a separator in order to prevent contact between that will lead to short circuiting. The separator is typically an electronically insulating microporous polymeric membrane that allows the movement of Li-ions between the two electrodes aided by the electrolyte. The electrolyte, while being electronically insulating and ionically conductive is in direct contact with the electrodes and separator and serve as a media for the Li-ions. The solid electrolyte interphase (SEI) is primarily formed in the first cycle and is created due to the reduction of the electrolyte [12]. SEI allows reversible Li-ion intercalation into the anode while preventing further electrolyte decomposition. The SEI layer formation is essential to the cycling stability and performance of LIBs. Figure 2.1 illustrates the basic working principles of a Li-ion battery. This basic design was commercialized by Sony and has not changed since. However, various types of electrode materials, electrolytes and separators have been explored over the years.

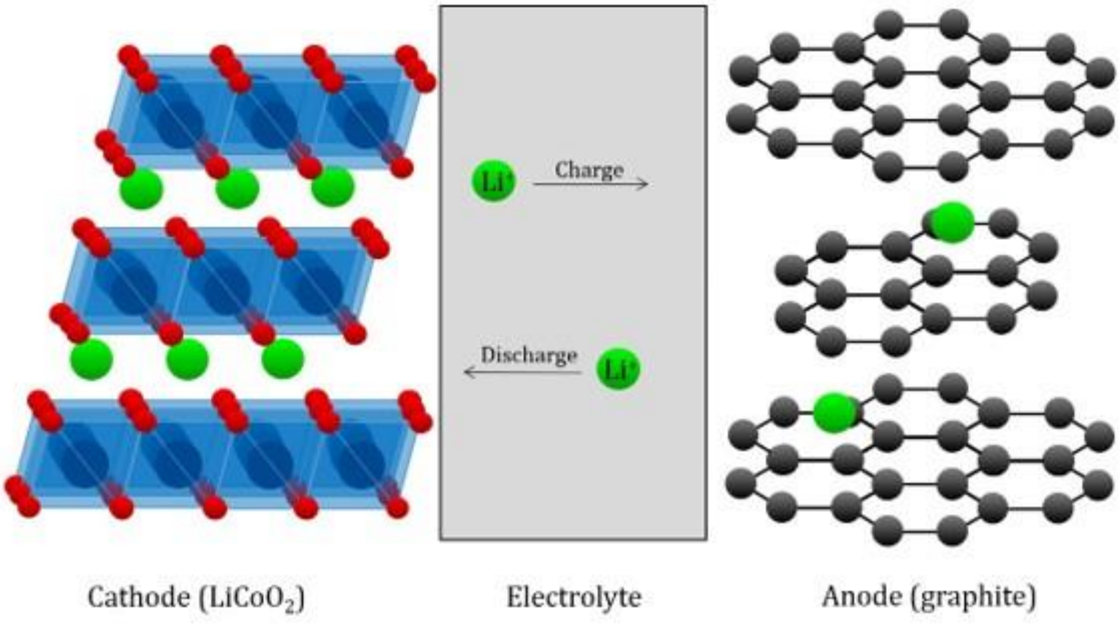

Figure 2.1: Schematic representation of the working principles of a LIB, using LCO as a cathode and graphite as anode. Li-ions move from the anode to the cathode through the electrolyte during discharge and electrons move through an outer circuit (not included in figure). This process is reversed during charge. Figure was retrieved from [13].

Schematic representation of the principles in a Li-ion battery, using LCO battery with graphite as anode. Li-ions move from the cathode to anode through the electrolyte during discharge and electrons move through an outer circuit (not included in figure). This process is reversed during charge. Figure was retrieved from

The basic principle of LIBs is so-called “rocking chair” mechanism, where Li-ions intercalate into the active materials of electrodes during the redox reactions. During discharge, Li-ions deintercalate from the lithiated graphite structure to form pure graphite and diffuses to LCO and the same number of electrons leaves the graphite structure and moves to LCO through an outer circuit, and the reverse reaction leads to intercalation of Li-ions into the structure to form LiC_6 according to the following reaction

$$Li^+ + e^- + 6C \leftrightarrow LiC_6 \qquad \text{Reaction 1}$$

On the cathode side, the intercalation and deintercalation occurs according to the following reaction (here LCO is used as an example)

$$LiCoO_2 \leftrightarrow 0.5Li^+ + 0.5e^- + Li_{0.5}CoO_2 \qquad \text{Reaction 2}$$

Commercial cells are assembled in discharged state as both the cathode materials and anode materials are thermodynamically stable in atmosphere and can easily be handled in industrial practices. During the first charge, the two electrodes are connected via an outer circuit to an external electrical supply. Electrons are forced to be released at the cathode and move via the outer circuit to the anode. In parallel, the Li-ions move simultaneously in the same direction from the cathode to the anode through the electrolyte keeping the electrical neutrality. In this way, the external energy is stored electrochemically in the battery in the form of chemical energy because of the difference in chemical potentials between the cathode and the anode. During discharge, the opposite process occurs. Electrons move from cathode to anode through the external load to do the work and Li-ions move from anode to cathode through the electrolyte. This is known as “rocking chair” mechanism, as Li-ions shuttle between the anode and cathode during charge and discharge [14]. This mechanism makes the batteries rechargeable, which is desirable for many applications and they also boast high voltage (3.6V for this type of battery with this selection of anode and cathode) and a theoretical specific capacity of 372 mAh g^{-1} for the graphite anode [14].

Different performance characteristics of batteries are capacity, energy, power and voltage. These relate to each other as shown in Equations 1-3, where U is voltage (V), C is capacity (Ah), E is energy (Wh) P is power (W), I is current (A) and t is time (h) [13].

$$voltage \cdot capacity = energy \rightarrow U \cdot C = E \qquad \text{Equation 1}$$

$$voltage \cdot current = power \rightarrow U \cdot I = P \qquad \text{Equation 2}$$

$$power \cdot time = energy \rightarrow P \cdot t = E \qquad \text{Equation 3}$$

Capacity is a property that describes how much charge a battery can store, and Ah is used as unit. Capacity is highly dependent on amount of material and is often reported as capacity per mass (gravimetric capacity) or volume (volumetric capacity) [13].

2.2 Characterization

2.2.1 X-ray diffraction (XRD) and pair distribution function (PDF)

X-ray diffraction is a characterization technique that utilizes the elastic scattering of X-ray photons by atoms located in a periodic lattice [15]. Therefore, it has to be a crystalline material to be studied, while amorphous materials will not give any distinct signals that can be studied. Crystalline materials have a repeating unit cell with a given periodicity for atomic positions that will either give constructive or destructive interference with the incoming X-rays. Figure 2.2 illustrates how crystal planes diffract X-rays and how this allows one to derive the lattice spacing using Bragg's law.

$$n\lambda = 2d \sin(\theta) \qquad \text{Equation 4}$$

where n is an integer called the order of reflection, λ is the wavelength of the incoming X-rays, d is the characteristic spacing between the crystal planes of a given sample and θ is the angle between the incident beam and the normal to the reflecting lattice plane. The interplanar spacings of every single crystallographic phase can be determined by measuring the angle, under which the constructively interfering X-rays leave the crystal.

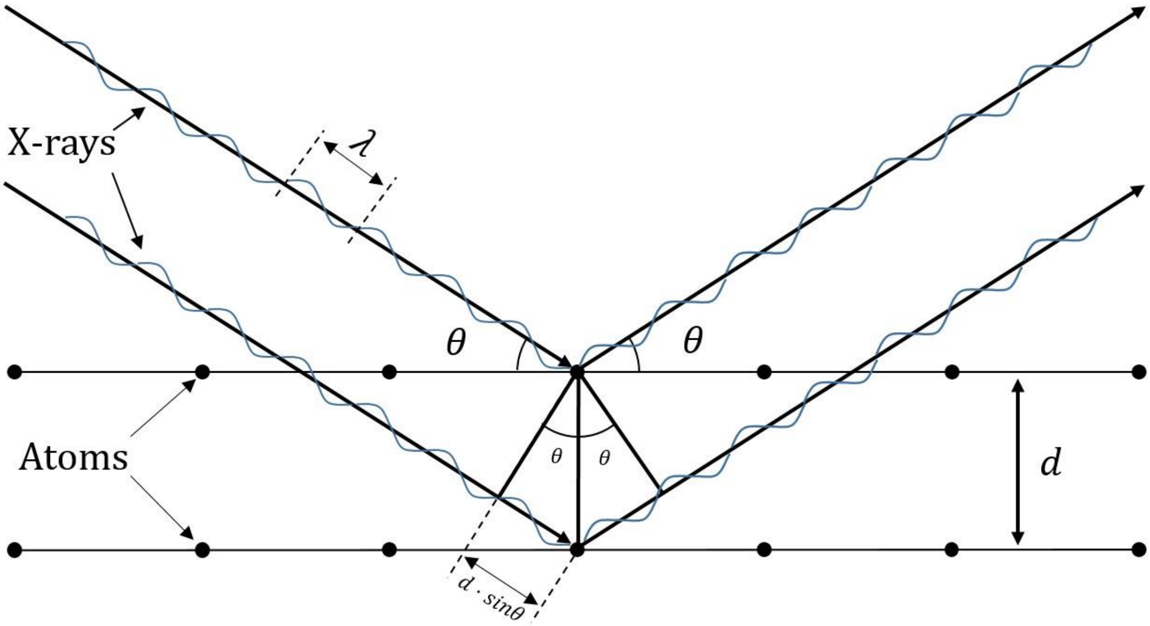

Figure 2.2 Schematic of Bragg's law showing the geometrical relation between the distance of imagined planes of carbon atoms (d), the wavelength of the X-rays (λ) and the angle between the X-rays and the atomic plane (θ). Figure was retrieved from [13].

The recorded powder diffraction data is then compared with the standard line patterns available for various compounds in the Powder Diffraction File database. Raw data acquired with this technique can be refined using the Rietveld method and TOPAS [16, 17].

Pair distribution function is derived from X-ray diffraction technique that describes the distribution of distances between pairs of articles contained within a given volume focusing on short range order [18]. Therefore, this technique is also able to analyse both crystalline- and amorphous samples. Distance between individual atomic pairs is considered. A number of neighboring atoms for a central atom is determined for increasing distance in all three dimensions. Close to the central atom, the probability of encountering an atom is low, while for a few radii the probability is high. Sweeping through the pair distances gives a probability distribution that is unique to the given atomic arrangement. According to theory, the probability pattern at small radii should have distinct features, while at larger radii the plot should level out and this is observed experimentally. Good resolution in the sharp featured short radii region is acquired by doing measurements at the highest possible angle and with the shortest possible wavelengths. Therefore, high energy tubes and wide angular range are needed.

2.2.2 Scanning electron microscopy (SEM)

Scanning electron microscopy is a technique where electrons are focused into a thin beam, down to 1 nm, to scan the surface of a sample [19]. This electron beam interacts with the sample and signals from these interactions can be measured with a detector. There are two main types of electrons that are detected in SEM: secondary electrons, and backscattered electrons, electrons reflected back after elastic interactions between the beam and sample, both o. Secondary electrons originate from inelastic interactions between the electron beam and the sample, and because of the limited energy of the emitted electrons we can only detect those that come from the surface. These are therefore best for studying the morphology of the surface. Backscattered electrons are reflected back after inelastic interactions between the beam and the sample. They have higher energy and can therefore provide information from a higher depth of the sample. These are more sensitive to atomic number of the elements and phase differences [20]. The two types of electrons resulting from interaction between the beam and sample is shown in Figure 2.3.

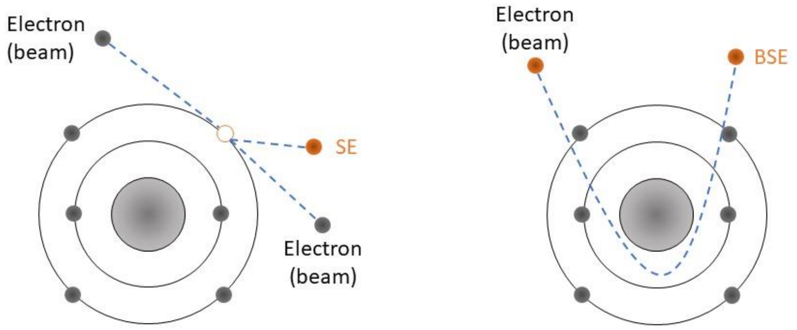

Figure 2.3: Illustration of secondary electrons (left) and backscattered electrons (right). Figure was retrieved from [20].

SEM is a valuable characterization technique that is able to provide imaging of particles, which can be used to determine particle size, distribution and morphology. Which in this work can aid in explaining the performance of different graphite samples.

2.2.3 Galvanostatic cycling (GC)

Galvanostatic cycling is an electrochemical characterization technique used to test the performance of batteries where a constant current is applied during charge and discharge, while the voltage is measured. The current is transitioning between positive and negative values as the cell is charged and discharged respectively. The applied current is decided relative to the active mass of the electrode and is given as mA g^{-1} in most cases or C-rate. C-rate is 1 divided by the number of hours required for full discharge of a battery, calculated from the theoretical capacity of graphite. For example, 1C equals 1 hour of discharge and 10C equals 6 minutes of discharge [13]. In most cases, actual capacity will be lower than theoretical capacity and therefore the calculated C-rate will differ from the actual C-rate. By multiplying the current with the discharge time, the capacity can be determined [13]. Information about the cycle life of a battery is obtained by cycling the battery and observing the change in capacity. The acquired data is then plotted to give information about the performance of the cell and the cell itself.

2.2.4 *Operando* X-ray diffraction

Operando XRD is a characterization technique that combines XRD measurements and electrochemical cycling of a battery. Thus, this powerful technique is used to monitor the chemical (structural) changes in the active material as it undergoes discharging or charging. Therefore, the different phases that form during cycling are detected while an electrochemical analysis is being performed. As a result, operando XRD allows to understand the electrochemical mechanisms in the cell. This technique requires a specialized cell that allows both cycling of the battery and also allows penetration of X-ray beams through the cell [21, 22]. A versatile configuration of a cell allows to evaluate the individual (cathode or anode) material in a half-cell configuration or a combination of materials in a full cell. The primary disadvantage of the characterization in a full cell is the overlap of the reflections corresponding to cathode and anode materials, which makes the data analysis more complicated. In the present work, *operando* XRD has been carried in a half-cell configuration with Li metal foil as a counter electrode

2.3 Graphite

Intercalation/deintercalation is the mechanism which is used to explain how Li-ions enter and exit layered structures during charge and discharge in LIBs. Researchers have been studying this mechanism extensively over the past decade to reveal the exact details of the intercalation mechanism and structural features of the intermediate stages that form when graphite is electrochemically cycled. Graphite has a highly oriented layered structure with a regular network of carbon hexagons. There are covalent bonds between carbon atoms (1.41 Å) within layers and weak van der Waals forces between graphene layers. These weak forces enable the intercalation of ions and even molecules between graphene sheets. As a result, graphite goes through several stages as it is filled with Li-ions during lithiation and emptied during delithiation. Rüdorff and Hofmann developed the model of such intercalation mechanism in 1938 [23], which explains that each "*n*th stage compound" fills up each nth layer with Li^+, as seen in Figure 2.5. For example, Stage 4 has every 4th layer filled with Li^+, while Stage 1 has every layer filled.

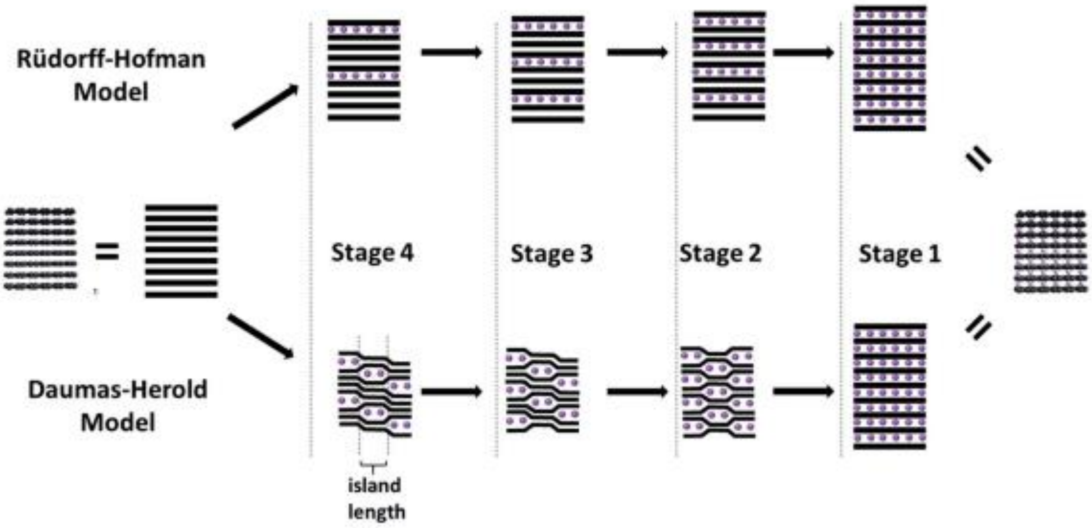

Figure 2.4: Two models for staging mechanism, Rüdorff-Hofmann model and Daumas-Herold model. Adapted from [10].

The staging phenomenon is related to the energy required to expand the gap between two graphene layers. This model has a crucial limitation that can't explain the transition from Stage 4 to Stage 2 through Stage 3, assuming that the layers span the entire graphite crystal and also empty layers during lithiation and delithiation, which is not realistic. Rüdorff and Hofmann discussed this limitation in their seminal work [23].

Specifically, this type of transitions (Stage 4 to Stage 3 and Stage 3 to Stage 2) would require deintercalation of a complete layer of Li-ions and the re-intercalation into a neighboring layer, since diffusion across the basal planes is not possible, and therefore was discarded. Several decades later, Daumas and Herold postulated a modified model to overcome the abovementioned limitation of the Rüdorff-Hofmann model [24]. The new model proposed that for all stages n>1, the graphene layers are flexible and, therefore, can deform around domains comprised on the intercalating atoms as seen in Figure 2.5. The domains are small compared to the crystallite size itself, and the layers are stacked according to the initial model suggested by Rüdorff and Hofmann, and the Daumas and Herold model still requires empty layers. As a result, the ordering mentioned in the staging mechanism is maintained locally. Therefore, the transition between Stage 3 and Stage 2 would occur when the intercalants diffuse within the same layer. Several studies provided experimental evidence for a domain-dominated structure for GIC according to the model proposed by Daumas and Herold. The evidence was based on simulations [25], scanning ion microprobe [26], high-resolution electron microscopy [27] or a combination of Raman spectroscopy and optical microscopy [28]. The staging mechanism itself remains to be fully elucidated and seems to be more complex than initially proposed even with the experimental evidence provided. As a result, the model predicts clusters of Li-ions forming “islands” evenly distributed throughout the structure. However, being derived from the Rüdorff-Hofman model, the Daumas-Herold model still carries some limitations – for instance, its inability to explain the transition from Stage 3 to Stage 2 and the occurrence of empty layers in the structure. The limitations of both models have puzzled the research community for years, making irony of the fact that graphite has been extensively used in commercial batteries.

In addition to these two models, Weng *et al*. proposed a new model to explain the intercalation/deintercalation mechanism and structural changes that occur in graphite during electrochemical cycling in LIBs. They also suggest a localized domain model that differs from the model proposed by Daumas and Herold, a key point being the absence of empty layers. Here, the localized domains are not evenly distributed and homogenous, but rather unevenly distributed and inhomogeneous microscopically as shown in Figure 2.6.

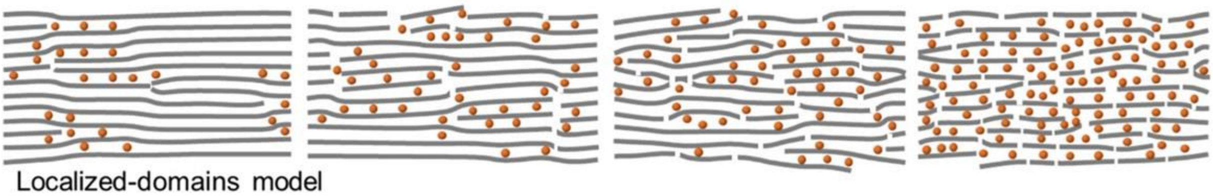

Figure 2.5: Schematic illustration of the lithiated graphite at different stages proposed by Weng et al. Adapted from [29].

This updated model shows that Li-ions distribute unevenly throughout the structure generating local stress and dislocations in the graphitic structure. The number of defects and dislocations increases with increasing concentration of Li-ions in the structure and delithiation mostly reverts the structure back to its starting point with some of defects remaining. The authors of the original work did not specify what type of defects are formed, nor the driving force behind the return to almost pristine graphite. Additionally, this model does not explain the ordering required to create the diffraction patterns of the different stages. It also does not explain why all the layers are perfectly aligned in the pristine graphite, but defects are generated in the structure during discharge. Without detailed explanation, it seems like C-C bonds are being broken, which does not seem realistic as the C-C bond is an aromatic bond that requires an enormous amount of energy to break. What could be the case here is that individual domains could be aligned in the pristine sample causing it to look like single layers form in the whole material, and during cycling these domains misalign causing defects to form at grain boundaries. Additionally, they state that the formations of defects are mostly reversible. During charge, the defects revert back and at 3 V, the structure is mostly back to the pristine state, with a defective fraction of 9.6%, but what is the driving force behind this? Another point to mention is that this is not *operando* TEM, therefore the measurements are from different electrodes and may vary, as we have seen for our own samples.

Despite the evident limitation of the proposed models, they have been adopted by the research community with a clear consensus that lithiation goes through a staging mechanism, where Stage 1 is the final stage for the Li-ion intercalation with an overall stoichiometry of LiC_6 being the highest Li-ion content at ambient conditions, resulting in theoretical capacity of 372 mA h g^{-1} and volumetric capacity of 850 mA h cm^{-3} [30]. The intercalation/deintercalation steps of Li-ions derived from the electrochemical measurements slightly vary from the general staging mechanism discussed above. With increasing Li-ion concentration in graphite, Stages *n*= 1L, 4L, 3L, 2L, 2 and 1 have been electrochemically observed as seen in Figure 2.7 a), and many conclusions have been drawn based on the electrochemical results. Here, ‘L’ indicates that the Li-ions are not ordered perfectly throughout the layers, but rather organized in a liquid-like disordered distribution [31]. However, the classification of the different stages varies in the literature. While some classify Stage 4 and Stage 3 as dense stages [10], others classify them as Stage 4L and Stage 3L meaning solid solutions [32]. Didier *et al.* ,with help of countless researchers over the last decade, mapped the different Stages of intercalation process in graphite [33].

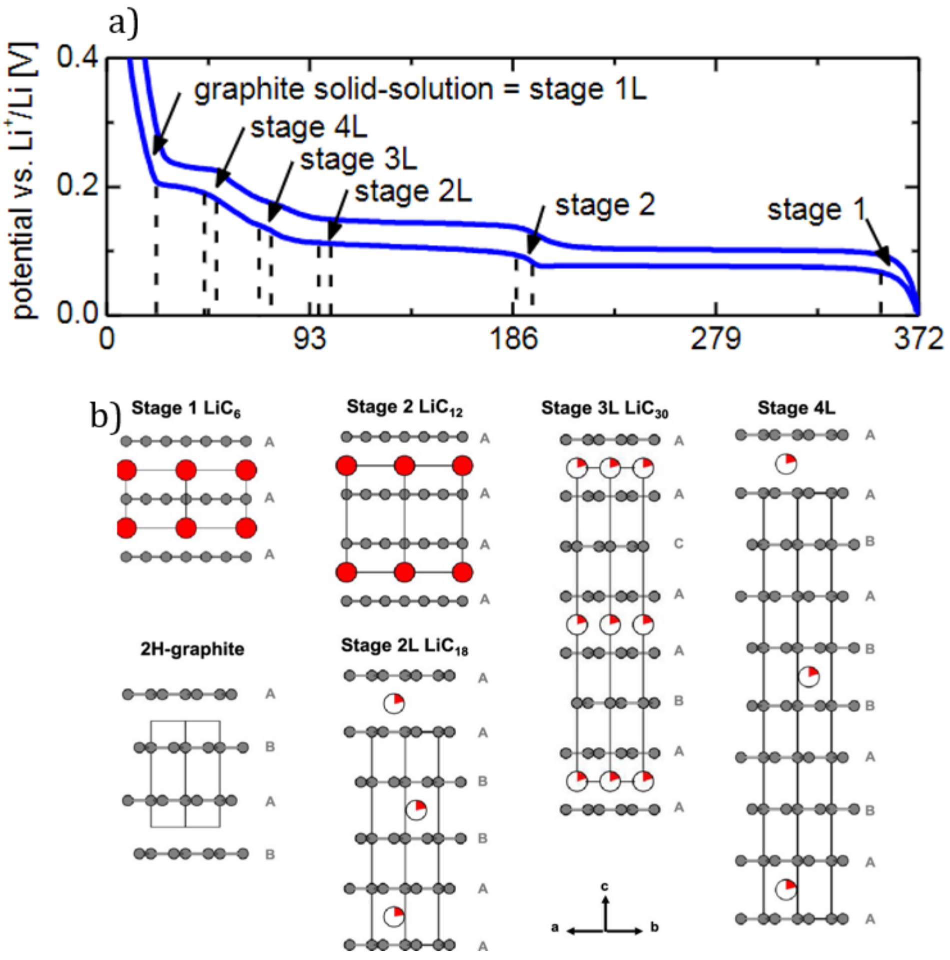

Figure 2.6: (a) Representation of crystal structure of Li intercalated graphite at intercalation stages showing the stacking organization of carbon layers along the [001] direction. Adapted from [33]. (b) Different stage and stage transitions of graphite during Li intercalation. Adapted from [32].

As a starting point of the model, the authors selected pure graphite, which adopts a 2H-Stage (hexagonal graphite with $P6_3/mmc$ space group) with staggered carbon layers in AB stacking sequence, as seen in Figure 2.7 b). Stage 1L occurs when 4-7% Li with respect to LiC_6 can be intercalated into graphite [31]. Here, every layer is filled with Li-ions in a liquid-like manner with no in-plane ordering, where the Li-ions are regarded as disordered and the environment around the Li remains to be fully solved. Here, AB stacking sequence is still adopted. Didier *et al*. claim that a first-order phase transition occurs to form Stage 4L from Stage 1L as more Li-ions intercalate into graphite, with every fourth interslab filled in a liquid-like manner, still lacking in-plane ordering [33]. The occurrence of the phase transitions is well monitored electrochemically by the appearance of multiple galvanostatic plateaus in sequence as depicted in Figure 2.7 a). The stage transition from Stages 4L, 3L and 2L have sloped decrease in potential, meaning an absence of a first-order transition, and the detailed mechanism is still not fully understood due to its complexity. The 4L Stage adopts a / ABAB/ BABA/, where the letters indicate the position of graphene layers and dashes indicate interlayers occupied by Li-ions [33]. With further increasing Li-ion content in the structure, Stage transition from 4L to 3L occurs and Stage 3L adopts /ABA/ ACA stacking, where the C-layer is shifted the same distance as the B-layer, but in opposite direction as seen in Figure 2.7 b). This stacking sequence was suggested by Billaud *et al*. through X-ray diffraction studies and study of different families of Bragg reflections [34]. The reported composition of this stage is LiC_{30} [35], and the transition between these two stages is still disputed. However, some authors demonstrate the existence of a two-phase region [36], while others report a continuous solid solution between the 3L and 4L phases [31]. With further lithiation, stage transition from 3L to 2L, and this new Stage adopts / AB/ BA stacking and LiC_{18} is the reported composition for the single-phase compound. Upon further intercalation, the structure adopts / AA/ AA stacking for Stage 2, where every other layer is occupied by Li-ions, and the reported composition is LiC_{12} [37]. Intercalation a step further yields Stage 1 with / A/ A stacking. All layers in the structures are occupied by Li-ions and the reported composition is LiC_6. Li-ions, in both LiC_6 and LiC_{12}, are ordered, where each Li-ion is facing the center of a carbon ring on each side of the interlayer. LiC_6 and LiC_{12} respectively, are the lithiated graphite structures that are well accepted.

Graphite and LiC_6 are well known phases, but there are problems associated with the data treatment of LiC_{18} and LiC_{12} from low quality XRD (X-ray diffraction) data due to peak overlap. To provide further insight, Missyul *et al*. conducted quantitative phase analysis of partially lithiated graphite anodes in order to prove the existence of LiC_{18} and LiC_{12} using low quality XRD data [38]. They fabricated a set of cells with varying state of charge (SoC) (0, 20, 40 and 50%) and performed XRD on the different samples. The XRD data was processed with the Rietveld method [16],to see the different phases that occur for the different SoCs. $\mathrm{d}Q/\mathrm{d}V$ peaks obtained from cycling of graphite shows that it is not possible to obtain pure LiC_{18} as the $\mathrm{d}Q/\mathrm{d}V$ peaks for $LiC_{30} \rightarrow LiC_{18}$ and $LiC_{18} \rightarrow LiC_{12}$ overlap. Their simplistic solution was to stop charging at SoC 40% in order to make sure that only LiC_{18} and LiC_{12} were present in the anode. Phases LiC_6, LiC_{30} and graphite are easily distinguishable due to their peak positions and intensities, but most of the peaks of LiC_{18} and LiC_{12} are strongly overlapped due to their similar lattice parameters. Additionally, the layered nature of graphite results in a very high-preferred orientation when graphite is cast on metal foil to make electrodes. a strong preferred orientation decreases the number of peaks suitable for phase and structural analysis, and stacking faults contribute to additional changes resulting in distortion of peaks. Their solution was to utilize full profiles to do structural refinement since it considers both peak positions and intensities. With this method, they were able to confirm the suggestion they made in the article that it is possible to prove existence of both LiC_{18} and LiC_{12} despite having peak overlap and using XRD data that is of lower quality, compared to synchrotron experiments. Some things to consider here is that the peak fittings were performed on a single peak, the evolution of the 002 graphite peak. The structures Missyul *et al*. propose for LiC_{18} ($P6_3mc$) and LiC_{12} (P6/mmm) have space groups that have no symmetry relation [38]. We will discuss this in further detail in Section 5.3.

A variety of *ex situ* measurements have been conducted to elucidate the structural changes of graphite during lithiation, however, the *ex situ* measurements are not always representative of the real changes in the system [39].*Operando* measurements (for batteries – measurements conducted during electrochemical cycling), are much more suited for elucidation of the chemical mechanism as these techniques do not require extraction of samples from the cells, but rather analysed the chemical changes in the original chemical environment. *Operando* XRD and *operando* neutron diffraction are well suited techniques to study the structural changes graphite undergoes during lithiation and delitiation. Therefore, a few publications describe the findings obtained through these powerful techniques. For instance, Schweidler *et al*. performed *operando* XRD analysed with Rietveld refinement to investigate the volume changes of graphite [40]. Majority of published Rietveld analysis is based on one peak, the 002 graphite peak [38, 40-43].The diffraction measurements were performed during electrochemical cycling of a graphite half-cell using Li metal foil as a counter electrode in the potential range between 5 mV and 1.2 V over three cycles. The measurements shows that 002 graphite reflection evolve during intercalation and deintercalation.

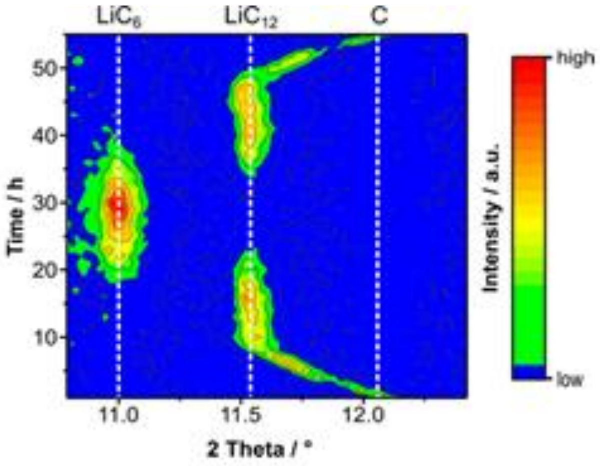

Figure 2.7: 2D operando XRD plot obtained during intercalation and deintercalation of Li-ions into graphite. The dotted lines illustrate the positions of the studied reflections for each of the well defined structure Adapted from [40].

The graphite 002 peak shifts to lower 2θ values during lithiation as graphite transitions to LiC_{12}, as seen in Figure 2.8. This shift is accompanied by significant variations in intensity and full width at half-maximum, indicating the appearance of dilute Stages 1L, 4L, 3L and 2L. The intensity of the 002 reflection strongly increases during the transformation from Stage 2L to Stage 2., with little change in peak position. For the transition from LiC_{12} to LiC_6, the 002 (in LiC_{12}) and 001 (in LiC_6) reflections coexist over a wider range of Li which translates into coexistence of both phases during intercalation. At later stages of lithiation, the 002 reflection corresponding to LiC_{12} becomes weaker until only the 001 reflection corresponding to LiC_6 remains. Their measurements also showed the change in interlayer spacing (*c*-axis evolution) when graphite is intercalated with Li-ions. The C to 2L transformation is characterized by a quasilinear change of the *c* lattice parameter. Closer inspection showed marginal changes in the slope of the *c*-axis evolution. Comparing with the plateaus in Figure 2 (b) indicates that these features can be assigned to the 1L to 4L, 4L to 3L, and 3L to 2L phase transformations. Interlayer distance is directly affected by the amount of Li-ions intercalated into the layered graphite structure. However, for the transition from Stage 2L to 2, the interlayer distance is rarely affected, as in-plane Li ordering rather than occupation of new layers dominates the intercalation mechanism in this region. After the system is further lithiated and passes the coexistence region of Stage 2 and Stage 1, the *c*-axis of Stage 2 levels off. In Stage 1, Li-ions are intercalated into every interlayer leading to a significant increase in interlayer distance as seen in Figure 2.8. The overall change they observed was 3.35 Å to 3.52 Å for the transition from C to Stage 2, and finally an increase to 3.7 Å as the transition to Stage 1 is completed.

Didier *et al*. explored the reversible lithiation of graphite in a commercial battery (cylindrical 18650 LIB from Panasonic) during cycling using *operando* neutron diffraction data collected every minute [33]. Like Schweidler *et al*., they observed a change in the interlayer distance as graphite was lithiated (Figure 2.9).

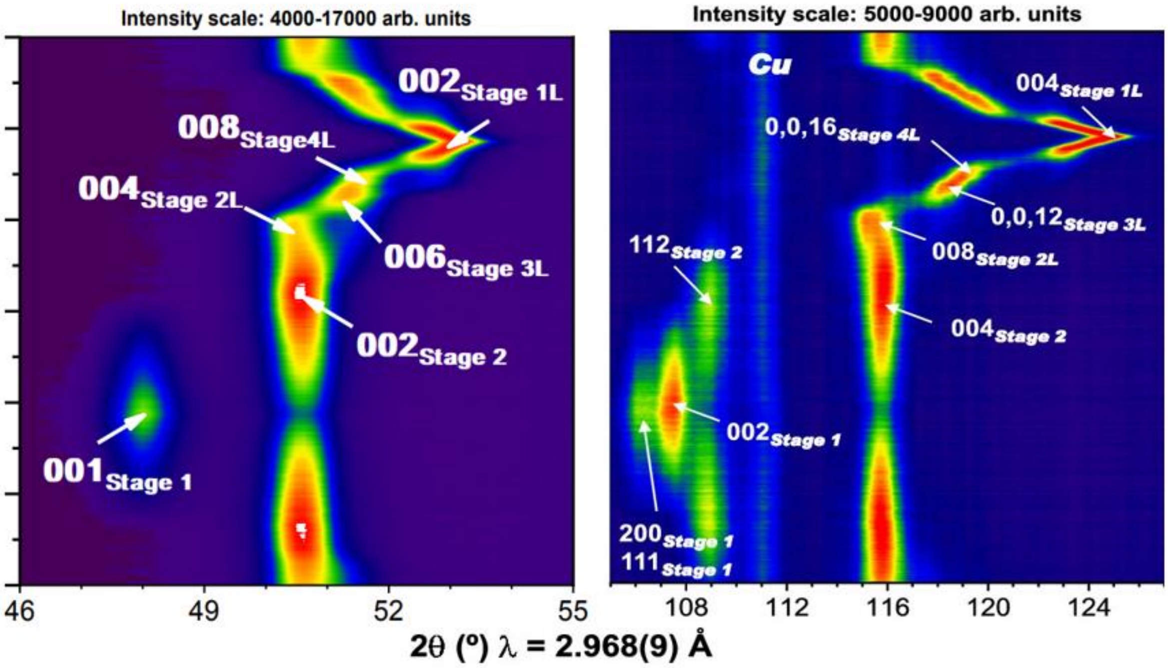

Figure 2.8: Operando neutron powder diffraction data over a selected angular range as a contour plot with intensity represented in color. Arbitrary count, where red is highest and blue is lowest, and white is off scale. Reflections from current collectors and GIC phases during discharge labeled with nominal compositions. Adapted from [33].

Additionally, the authors show film plots of the *operando* diffraction data (Figure 2.9) in time/SoC vs 2θ and labeled the peaks with Miller indices for the different stages and these Miller indices differ from those described by Missyul *et al*., which are [38]. The nominal compositions assigned in this work are: Stage 1 - LiC_6, Stage 2 - LiC_{12}, Stage 2L - LiC_{18}, Stage 3L - LiC_{30}. They mainly looked at the most intense LIG (Li intercalated graphite) phase reflections, being first- and second order 00*l* reflections observed in the ranges $45^\circ < 2\theta < 56^\circ$ and $104^\circ < 2\theta < 107^\circ$. Other LIG reflections were present, but had substantial overlap with reflections from other battery components as NMC-based cathode, Al- and Cu current collectors. By looking at the diffraction data, they were able to see differences between discharge and charge.

As the authors were looking at the transition between Stage 1 and 2, they noticed that the average interlayer distance remains almost constant in both phases, but a variation of the LIG phase reflection position exhibiting asymmetric behavior between charge and discharge was observed during the two-phase region. The magnitude of the changes were not significant according to the extracted standard uncertainty, but the trend of absolute values during charge and discharge was consistent with what Senyshyn *et al*. reported previously [44]. During charge, the interlayer distance of the Stage 2 phase changes from 3.508 Å to 3.510 Å in the composition range $0.40 < x < 0.79$. This occurs at the beginning of the two-phase transition and then appears unchanged during the transformation on charge, and then changes from 3.510 Å to 3.508 Å during discharge in the same region of x. The Stage 1 phase exhibits a decrease in the absolute magnitude of interlayer distance at $x \approx 0.79$ at the start of discharge, and this slowly recovers during the rest of the discharge. Variation in interlayer spacing suggested narrow composition ranges for Stage 1 and Stage 2. Didier *et al*. concluded that the observed changes were not significant enough, as theoretical calculations show that Stage 1 compounds with other compositions than LiC_6 are not thermodynamically stable. Stage 2L with reported composition of LiC_{18} was observed in the region between Stage 2 and 3L. This composition was observed during discharge, but not charge and is consistent with previous powder diffraction observations [45, 46]. On charge, the interlayer distance is vastly different from the one at discharge, remaining almost constant at 3.509 Å. An indication of absence or low amount of the Stage 2L phase during charge. They additionally found asymmetric behavior of Stage 2 and 2L phases, Stage 3L and 4L phases, and Stage 4L and 1L. The asymmetry being more significant for structures adopted at higher stages. These observations were consistent with other electrochemical measurements [32, 47]. The authors observed here that there is asymmetry between lithiation and delithiation, and this means that the lithiation- and delithiation mechanism differs. This point will be brought up in section 5.3.

In summary, graphite as battery material has been extensively researched throughout the last decade. Despite the materials simplicity, many things about the material remain shrouded in mystery. The following work will hopefully shed some new light on the uncertainties behind the lithiation/delitiation mechanism and structural changes of graphite that occur during cycling.

3. Experimental

3.1 Chemicals and electrolytes

Chemicals, powders and additives for electrolytes used in this work is listed in Table 3.1, they were obtained from commercial sources or partners and used without any additional chemical modifications. The graphite samples were obtained through MoZEES. Overview of chemicals, powders and additives for electrolytes.

Overview of chemicals, powders and additives for electrolytes. Listed with name, chemical formula, producer, purity and CAS-number.

Table 3.1: Overview of chemicals, powders and additives for electrolytes. Listed with name, chemical formula, producer, purity and CAS-number.

NAME	CHEMICAL FORMULA	PRODUCER	PURITY	CAS-NUMBER
S-201126-00088 (G1)	C	-	-	-
S-210308-062574 (G2)	C	-	-	-
S-191009-00048 (G3)	C	-	-	-
S-211108-000840 (G4)	C	-	-	-
Carboxymethyl cellulose sodium (CMC)	$C_8H_{15}NaO_8$	MTI	≥99.5%	9004-32-4
SUPER C65	C	Imerys	-	-
Styrene-Butadiene Rubber (SBR)		MTI	-	9003-55-8
Distilled water	H_2O	Produced at UiO		-
Li metal foil	Li (disc) Thickness: 0.4 mm Diameter: 15.5 mm	-	-	-
Lithium hexafluorphosphate	$LiPF_6$	Merck		
Ethylene carbonate (EC)	$C_3H_4O_3$	-	-	-
Ethyl methyl carbonate (EMC)	$C_4H_8O_3$	-	-	-
Vinylene carbonate (VC)	$C_3H_2O_3$	-	-	-
Fluoroethylene carbonate (FEC)	$C_3H_3FO_3$	-	-	-

Two types of electrolytes were used in this work. Table 3.2 shows name of electrolyte, salt added, solvent and additives.

Table 3.2: Overview of electrolytes used in the batteries. Listed with name, molarity, salt, solvent and additives.

NAME	Molarity (mol/L)	SALT	SOLVENT	ADDITIVES
E1	1.2	$LiPF_6$	EC:EMC (3:7/vol)	VC (2 wt.%)
E2	1.2	$LiPF_6$	EC:EMC (3:7/vol)	VC (2 wt.%) + FEC (10 wt.%)

3.2 Characterization of materials

3.2.1 Scanning electron microscopy (SEM)

The SEM-studies were performed on pristine graphite samples using an SEM of the type Hitacji SU8230 Ultra High Resolution Cold FE-SEM. These powder samples were put on electrically conductive carbon tape and placed on a sample holder. An accelerating voltage of 2 kV was used for all the imaging, and the pictures were taken with a detector for secondary electrons.

3.2.2 X-ray diffraction (XRD)

Graphite samples were packed into an 0.5 mm Hilgenberg glass capillary and sealed using UV activated glue. The made capillaries were then loaded into RECX-2 located at RECX lab at UiO and measured using a using a D8-A25 powder diffractometer with a Cu radiation source with a wavelength (λ) of 1.5418 Å for 4 hours. The capillaries rotated as the measurements was performed

3.3 Battery fabrication

The following section explains the methods used to make the graphite electrodes and assemble the coin cell batteries for electrochemical evaluation.

3.3.1 Electrode preparation

The first slurry was made using an in-house procedure made by our group. This slurry, and all others, was made in a mixing machine produced by Thinky ® (ARE 250). 3 wt% CMC and 2wt% CB of the total mass of the powder and 1.5 g distilled water (first row in Table 3.3) was weighed directly into a small mixing cup and mixed for 3 min at 2000 rpm. 95 wt% graphite (0.9538 g) was added and mixed for 10 min at 2000 rpm. Cu-foil was placed on a K Control Coater produced by RK Print. The slurry was casted with 500 µm wet thickness, dried in an oven at 60°C for 1 hour and dried in vacuum overnight at room temperature. The next day, we calendared the electrode and measured the thickness afterwards. The electrode sheet was cut into individual discs with 15 mm diameter using a handheld electrode cutter (Nogami). These cut electrodes were dried in a Büchioven under vacuum at 60°C for 4 hours to remove moisture and air from the electrodes before they were taken into a LABmaster SP glovebox from MBRAUN with Argon atmosphere of purity ≥99.999% (AR 5.0) and O_2- and H_2O levels below 0.01 ppm.

All other slurries (row 2-6 in Table 3.3) were made using an SOP we acquired through MoZEES. 1.1 wt% CMC (0.0109 g) and 1 wt% CB (0.0101 g) of the total mass of the powder in the slurry was weighed into a small mixing cup. Approximately 1.47 g of distilled water was weighed directly into the cup. The mixture was mixed for 10 minutes at 2000 rpm. A visual inspection was done on the slurry after the program ended to see if all CMC had dissolved. A small amount of CMC would in most cases be stuck to the bottom of the cup. The unmixed CMC was loosened with a spatula and the slurry was mixed for an additional 2 min at 2000 rpm to dissolve the remaining CMC. 95.6 wt% (0.9561 g) graphite was added to the cup and mixed for 10 min at 2000 rpm. The cup rested for 10 min with lid on to prevent solvent evaporation. The slurry was visually inspected after the rest to ensure all the graphite had mixed well into the slurry. Additional mixing and rest were done if needed. When the slurry was mixed well enough, 2.3 wt% SBR (0.244 g) was weighed directly into the cup and mixed for 3 min at 1000 rpm.

Cu-foil (produced by Mitzu) was taped onto a glass plate and the slurry was cast onto the foil right after the mixing program ended using metal bars with fixed heights. 200 µm, 300 µm and 500 µm were the height that were used. After casting, the foil was transferred onto a glass plate and dried inside a vacuum oven at 60°C at regular atmosphere for 1 hour. Then temperature was turned off and vacuum was pumped inside the oven. The following day, the electrode sheet was taken out and the thickness of the sheet was measured using a lab think C640 thickness tester to see if the coating was even. After the initial thickness measurement, the electrode sheet was calendared to 80-95 and the thickness was measured again to see if the wanted thickness was achieved. The electrode cutting and transfer steps are the same as those explained above

Table 3.3 shows the different quantities that were weighed out when making the different slurries and the average thickness of the electrode sheet after calendaring.

Table 3.3: Overview of weights of components used for slurries and measured thickness of electrode sheets aster calendaring. Listed according to electrode sheet.

ELECTRODE SHEET	CMC	CB	C	SBR	WATER	AVG THICKNESS
AT_T1	0.0328 g	0.0199 g	0.9538 g	-	1.5 g	120.0 µm
AT_T17	0.0110 g	0.0102 g	0.9565 g	0.0290 g	1.4472 g	98.3 µm
AT_T19	0.0111 g	0.0100 g	0.9560 g	0.0237 g	1.4772 g	86.9 µm
AT_T20	0.0109 g	0.0104 g	0.9562 g	0.0226 g	1.4760 g	89.8 µm
AT_T22	0.0109 g	0.0099 g	0.9555 g	0.0223 g	1.4773 g	88.8 µm
AT_T29	0.0110 g	0.0100 g	0.9562 g	0.0234 g	1.4774 g	95.7 µm

3.3.2 Battery assembly

Graphite, as an anode material, was here tested in half-cell type coin cell batteries shown in Figure 3.1. Here, graphite was the active electrode, while Li-metal was the counter electrode.

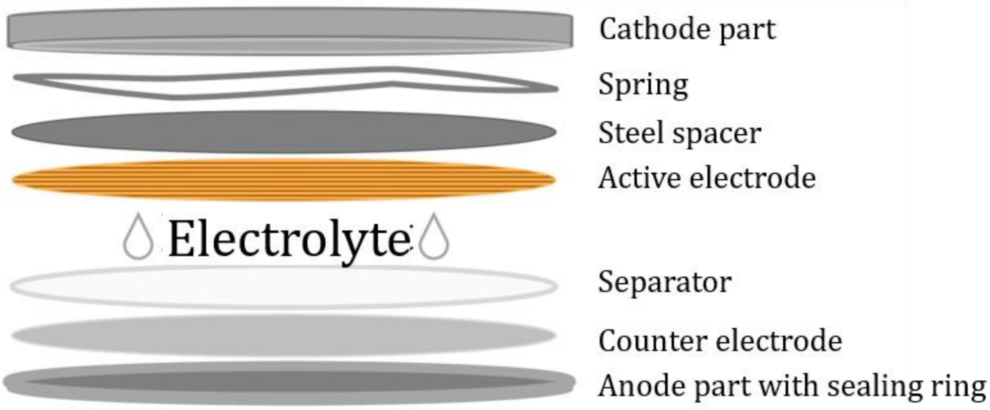

Figure 3.1: Schematic of half cells. Adapted from [48].

The coin cells (CR2932, stainless steel 304, Pi-Kem) were assembled inside the glovebox. The surface of a pre-cut Li metal foil was brushed with a toothbrush (First price, medium stiffness brush) to both increase the surface area and get a clean surface. The Li metal foil was then placed in the anode part of the coin cell with a glassmicrofiber separator (Whatman GE, 16 mm) on top. The graphite electrode was weighed on a XA105 DUalRange digital scale from Mettler Toledo, with an uncertainty of ± 0.1 mg inside the glovebox. The electrolyte was added after the weighing to minimize electrolyte evaporation. Then, the graphite electrode was placed graphite side down on top of the wetted separator followed by the steel spacer and the spring before the cell was closed with the cathode part. The assembled coin cell was sealed using an automatic press from Hohsen.

3.4 Characterization of batteries

3.4.1 Galvanostatic cycling (GC)

Galvanostatic measurements were performed on two different instruments. A CT-4008T-5V10ma-164 (Neware) battery tester placed in a room with aircondition temperature control and a MIHW-200-160CH (Neware) battery tester with a temperature chamber. The cells were tested in two voltage windows, either 0.01 to 2 V or 0.005 V to 2.0 V against Li/Li^+ and two different current densities were used for the GC measurements, 50 mAh g^{-1} and 100 mAh g^{-1}.

3.4.2 *Operando* X-ray diffraction

The *operando* measurements were done at the X-ray lab located at the Department of Chemistry at University of Oslo. The *operando* measurements were done with RECX-2 using a D8-A25 powder diffractometer with an Mo K-alpha radiation source with a wavelength (λ) of 0.71076 Å, focusing mirror optics, Eiger 500 K 2D area detector and a Biologic SP150 battery cycler. X-ray diffraction data was collected in still scan mode using the entire detector giving a scan range from 9-27° in 2θ. A special electrochemical cell designed for performing *operando* XRD experiments in transmission mode was used for the *operando* measurements, and is shown in Figure 3.2. We used glassycarbon windows instead of sapphire windows for our cells, and the glassy carbon windows were glued onto the cell with conductive silver paste.

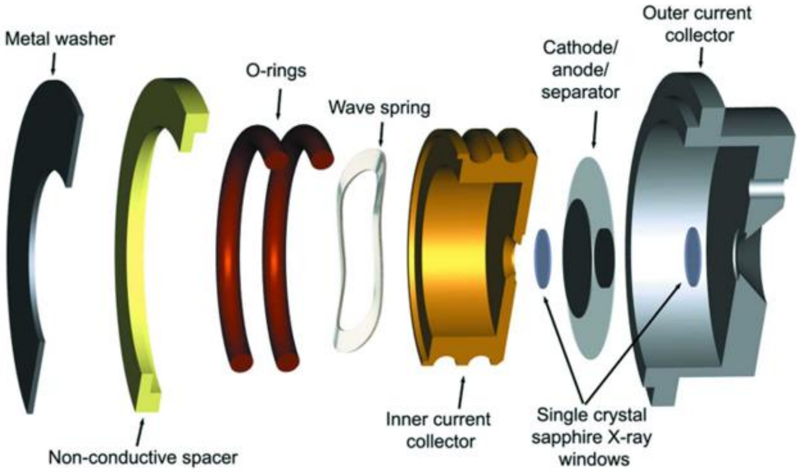

Figure 3.2: Schematic drawing of an operando cell used for our experiments. Adapted from [22].

The measurement cell was constructed with an inner- and outer current collector. Two O-rings are used to both prevent contact between anode and cathode, but also to fully seal the cell to prevent contact with the outer atmosphere. The battery was fabricated between the current collectors as seen in Figure 3.1 similar to the explanation in section 3.3.2. fabricated on the outer current collector with Li metal foil, separator, electrolyte and graphite electrode in the given order. The same electrolyte and electrodes, with current collector, were used here as for the coin cells.

GC was used as the electrochemical characterization technique for *operando* XRD. 50 mAh g^{-1} and 100 mAh g^{-1} current densities were used in the voltage window 0.01 to 2 V and each X-ray scan lasted 5 or 10 min and measured in range 1.29 to 4.23 Å^{-1} (11-26°). The acquired data was processed using Python, used scripts can be found in Appendix.

The *operando* plots were made by plotting the X-ray diffractograms with the same x-axis, the diffractogram scan number was the y-axis and the intensity was shown with color that corresponded to low- or high intensity.

Multiple samples were also measured at BM=! Beamline, which is a part of the Swiss-Norwegian beamlines (SNBL), at the European Synchrotron Radiation Facility (ESRF) with different C-rates of C/20, C/6 and C/2. SP150 battery cycler (Biologic) was used for the GC measurements and operando measurements were performed with a Dectris Pilatus 3X 2M CdTe detector with wavelength of 0.69024 Å

3.4.3 Pair distribution function (PDF)

Coin cells were cycled and stopped at different voltages during lithiation and delithiation. The cells were opened, and the electrodes were taken out inside the glovebox and left to dry for some hours. Afterwards, the electrode material was gently scraped off the Cu-foil using a metal spatula and mortared. The mortared powder was packed into a 0.5 mm capillary inside a LABmaster SP glovebox from MBRAUN with Argon atmosphere and sealed using UV activated glue. These samples were measured at ESRF with a Dectris Pilatus 3X 2M CdTe detector with wavelength of 0.31916 Å.

4. Results

4.1 XRD characterization

The graphite samples used in the present work were obtained from multiple sources through MoZEES. All of them were either natural or synthetic graphites and had varying domain sizes and surfaces. Samples G1, G2 and G4 were synthetic, while sample G3 was natural graphite. Therefore, initial characterization was necessary to get information about their crystallinity. *Ex situ* XRD was performed on all the samples and their corresponding XRD patterns are shown in Figure 4.1.

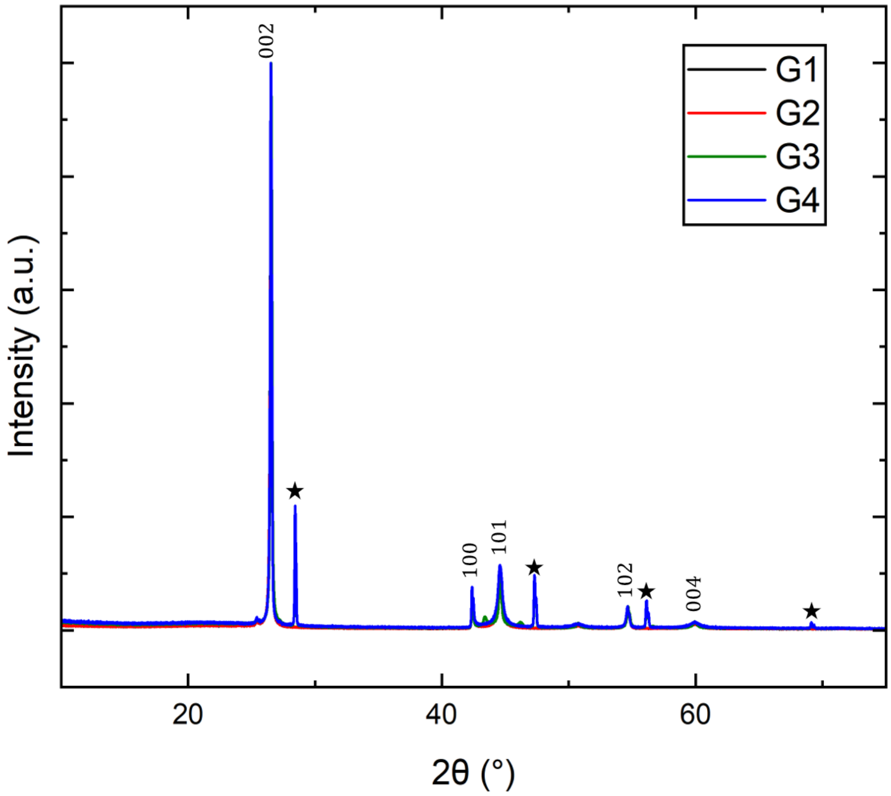

Figure 4.1: XRD patterns for samples G1 (black), G2 (red), G3 (green) and G4 (blue), and the different graphite peaks are marked with Miller indices.

The presented results were normalized by dividing with the largest value in each respective sample measurement. We see that all the samples have the same graphite peaks appearing, with no detectable traces of impurities, except for G3 that has 2 small unidentified peaks around 43° and 47°. This is probably because it is natural graphite, which is difficult to make completely pure. The graphite peaks are marked with their corresponding Miller indices 002 (26.5°), 100 (42.4°), 101 (44.6°), 102 (54.7°) and 004 (60.1°). The peaks marked with a black star originate from the silicon reference we added to correct any peak shift that could have occurred during measurements or measurement setup.

4.2 SEM characterization

After determination of the crystal structure, it was important to examine the morphology of graphite particles as it can have a large influence on the electrochemical performance [49]. Thus, all samples were examined using SEM to understand their differences.

The SEM pictures of sample G1 in Figure 4.2 shows a wide variety of graphite particles with different shapes and sizes. Mostly in range of 4.5 to 25 μm. Both smaller and bigger particles demonstrate a significant degree of aggregation. Additionally, there are two main type of surfaces that can be seen in this sample: smooth and flaky surfaces. The surfaces are either flat or rounded for majority of particles, that can be seen in the presented view. A minor set of particles have holes in the surface, and a few are structured with plate like-particles stacked on top of each other.

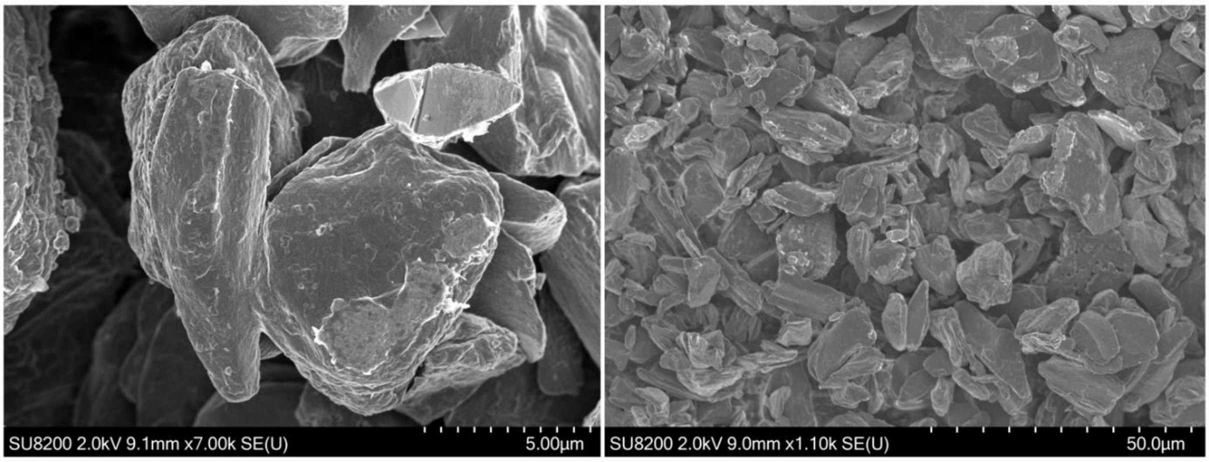

Figure 4.2: SEM pictures of synthetic graphite sample G1, captured with an accelerating voltage of 2 kV.

Figure 4.3 shows SEM images of sample G2, which also shows large variation in particle size and shape. Both small and large single particles are present in addition to aggregates. We see particles vit varying size from 10 to 60 μm. The surface of most of the singular particles are relatively smooth, but smaller flakes can be seen on the surface. Both flat and rounded surfaces occur for this sample and graphite plates stacked on each other forming a larger particle is seen in this sample

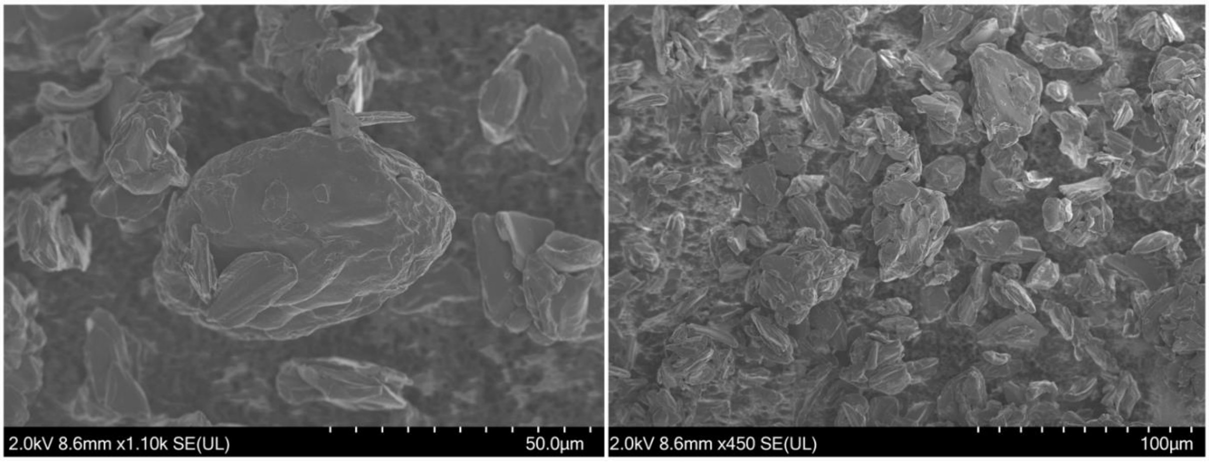

Figure 4.3: SEM pictures of synthetic graphite sample G2, captured with an accelerating voltage of 2 kV.

SEM pictures of natural graphite sample G3 are shown in Figure 4.4. The particle sizes also vary greatly here. However, the spheroidization process with further surface treatment was conducted differently for this sample and the particles are less prone to aggregation, as could be observed for some particles in Figure 4.2 (Gr1). There are some indications of particle aggregates in the image, but difficult to determine as it could be a result of particles laying close together. Here, particle sizes vary from 10 to 25 µm. A higher number of rounded particles is observed for this particular sample and uneven surfaces dominate in the sample. The flakes observed on the surface of the graphite particles vary in shape and size. Upon further inspection, cavities are seen that allow view into the particle and some of the cavities show a layering of larger graphite plates.

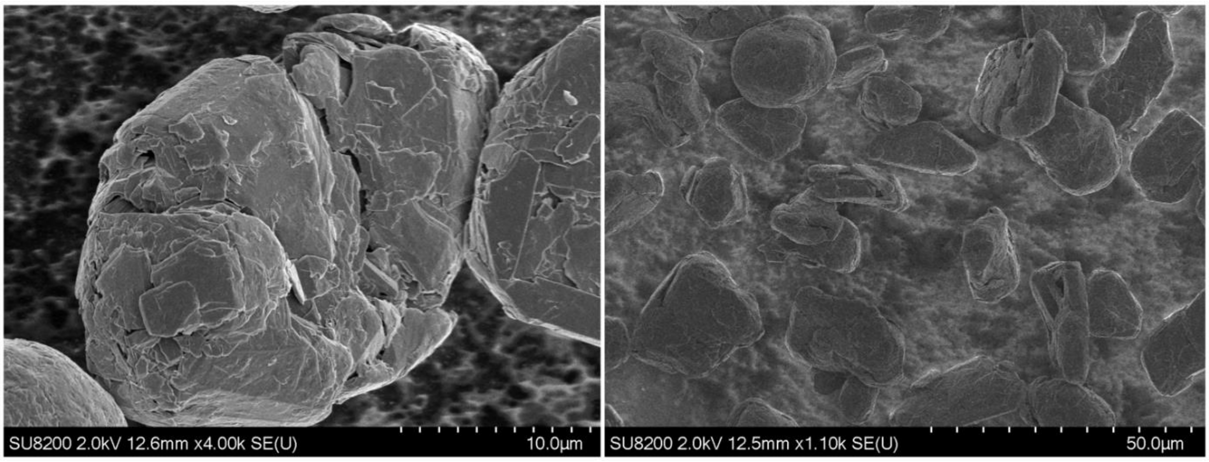

Figure 4.4: SEM pictures of natural graphite sample G3, captured with an accelerating voltage of 2 kV.

Figure 4.5 shows SEM images of sample G4, which is somewhat similar to the other samples. The main difference between this and the other samples is that majority of the particles are made up of larger flakes stuck together in a layering type of structure. Due to the plated structure, it becomes difficult to determine which particles are stuck together and which ones constitute only a single particle. However, it is possible to see some particles that are stuck together. This sample has particle sizes varying from 4 to 40 µm. Many particles have flat planes covering most of the surface with different elevation due to the size of the plates. A minority of round particles, that are similar to those seen in Figure 4.2 (G1), with a flaky type of surface are also found in this sample.

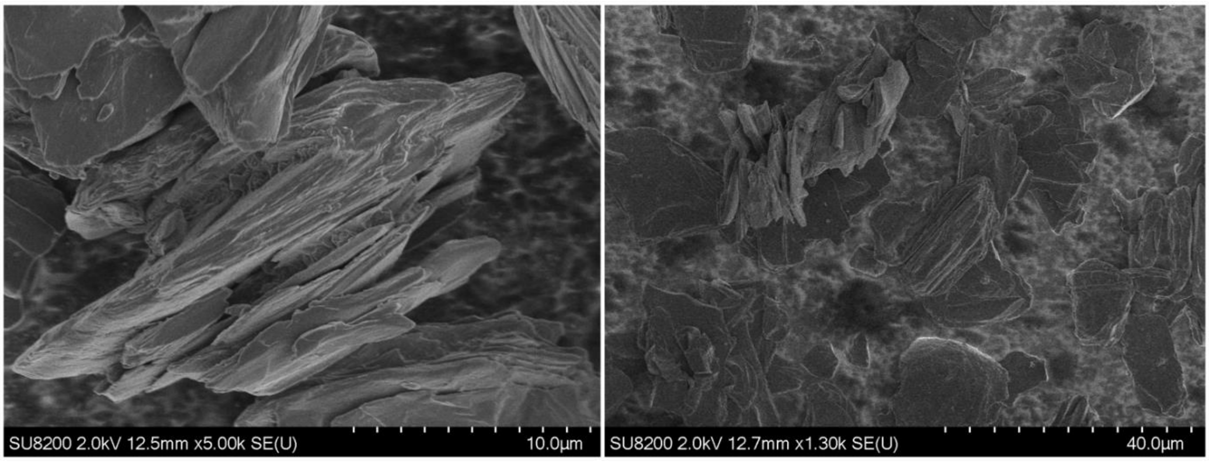

Figure 4.5: SEM pictures of sample G4, captured with an accelerating voltage of 2 kV.

4.3 Optimization of electrochemical performance

This section is dedicated to the optimization of the electrochemical performance of the graphite-based anodes, characterized with galvanostatic cycling measurements conducted on half-cells with Li metal as counter. Table 4.1 shows an overview of the cells that are presented in this section, and they are listed in the order they are presented. Here the battery names are listed with corresponding active mass, OCV before cycling and which type of graphite that was used in the cell.

The aim of this part of the work was to obtain stable electrochemical performance of the graphite, to observe how prolonged cycling would affect the chemical mechanism of the material.

Table 4.1 Overview of coin cells presented in Section 4.3 listed with name, active mass, starting voltage and type of graphite used.

BATTERY NAME	ACTIVE MASS	STARTING VOLTAGE	Graphite sample
AT_T1_2	14.9 mg	2.35 V	G1
AT_T1_3	15.5 mg	1.68 V	G1
AT_T17_67	16.0 mg	2.85 V	G1
AT_T17_68	16.7 mg	2.71 V	G1
AT_T17_69	16.6 mg	2.82 V	G1
AT_T22_73	14.4 mg	3.09 V	G2
AT_T22_74	14.6 mg	2.94 V	G2
AT_T22_75	14.8 mg	1.26 V	G2
AT_T19_79	16.1 mg	3.11 V	G3
AT_T19_80	16.2 mg	3.08 V	G3
AT_T19_81	16.4 mg	1.88 V	G3
AT_T29_130	15.0 mg	2.29 V	G1
AT_T29_131	14.7 mg	2.82 V	G1
AT_T29_132	15.2 mg	2.88 V	G1
AT_T20_82	14.8 mg	3.04 V	G4
AT_T20_83	14.6 mg	1.78 V	G4
AT_T20_84	14.8 mg	0.76 V	G4

Graphite sample G1 (synthetic graphite) was the first sample we tested as an active material in half-cells. We used 1.2 M $LiPF_6$ in EMC:VC (E1) as an electrolyte for all the following cells. The electrode sheet was coated with a wet thickness of 500 μm and thickness after calendaring varied from 120-130 μm. Figure 4.6 show some of the first cells fabricated with the in-house procedure made by our group, where 3 wt% CMC, 2wt% CB, 95 wt% graphite (1 g total of solid material) and 1.5 g distilled water were mixed together for 3 min and 10 min at 2000 rpm.

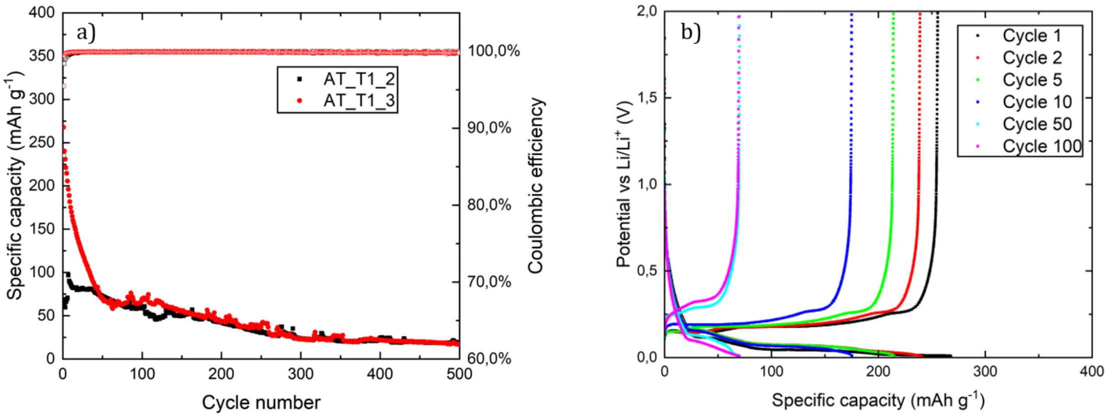

Figure 4.6: a) comparison of GC measurements for cells AT_T1_2 and AT_T1_3 displaying the change in specific capacity against cycle number and coulombic efficiency is displayed at the top of the figure. b) shows a representative GC plot for cell AT_T1_3. Electrolyte E1 was used in cell fabrication and voltage window 0.01-2.0 V vs Li/Li$^+$ was used for the GC measurements.

There was a slight variation in the active mass of the different cells. Cell AT_T1_2 and cell AT_T1_3 had an active mass difference of 0.6 mg. The current density was 100 mA g^{-1} and the voltage window was 0.01-2.00 V vs Li/Li$^+$. We decided early on to monitor the long-term stability, and study possible changes in the cycling mechanism of the graphite samples. Therefore, used a cycling program with 500 cycles for most of the cells we tested. As seen in Figure 4.6, the capacity is lower than the theoretical capacity and the overall capacity rapidly drops, which is an indication of the cell not working optimally. The reason could be due to different factors in the slurry process, cell fabrication or cycling. Therefore, optimization was necessary to improve the performance of the cells before we could utilize more advanced characterization techniques.

We made changes to the mixing procedure, by implementing dry mixing of CMC and CB using a metal spatula and ensuring that all CMC was dissolved before progressing to the next steps of the slurry making. The coating procedure was changed, and we decided to coat with 300 µm to get a lower mass loading on the electrodes as thick electrodes and high mass loading could be a factor that caused the first cells to perform poorly. We also started taping the foil to the glass plate rather than using ethanol to fasten it to the glass plate, which made it easier to transfer the electrode sheet into the oven for drying and prevented crumping of the electrode sheet during transfer. Figure X.X shows a selection of GC measurements from electrode sheet AT_T17.

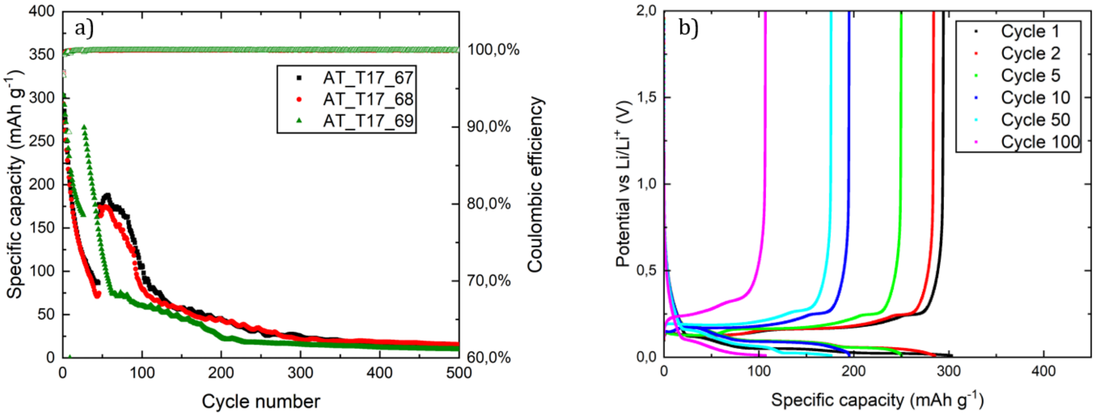

Figure 4.7: a) comparison of GC measurements for cells AT_T17_67, AT_T17_68 and AT_T17_69 displaying the change in specific capacity against cycle number and coulombic efficiency is displayed at the top of the figure. b) shows a representative GC plot for cell AT_T17_67. Electrolyte E1 was used in cell fabrication and voltage window 0.01-2.0 V vs Li/Li$^+$ was used for the GC measurements.

This set of cells were cycled with a current density of 50 mA g^{-1}. Cells AT_T17_67, AT_T17_68 and AT_T17_69 had active masses between 16.0-16.7 mg and only had slight variation in their OCVs. Here, all the cells have similar starting capacity (still lower than the theoretical capacity). The cells follow a similar trend despite minor differences and have a large increase in capacity around 50 cycles, which we did not observe for the previous cells with graphite sample G1. We observed similar behavior for cells fabricated from electrode sheets AT_T22 (graphite sample G2) and AT_T19 (graphite sample G3). The electrochemistry data for cells fabricated with electrodes from AT_T22 and AT_T19 is presented in Figure 4.8.

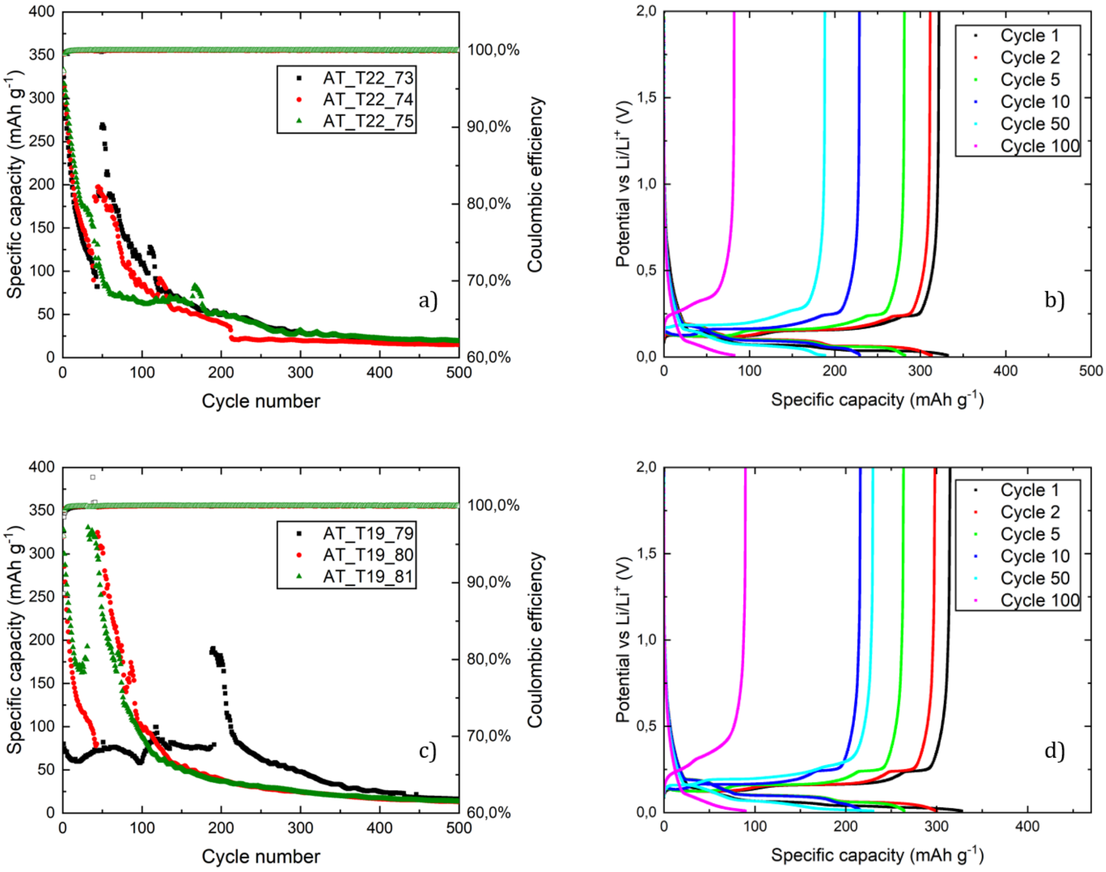

Figure 4.8: a) GC measurements for sample G2 and b) shows representative GC measurement for cell AT_T22_74. c) GC measurements for sample G2 and d) shows a representative GC measurement for cell AT_T19_81. Electrolyte E1 was used in cell fabrication and voltage window 0.01-2.0 V vs Li/Li$^+$ was used for the GC measurements.

Cells AT_T22_73, AT_T22_74 and AT_T22_75 (Figure 4.8 a)) and cells AT_T19_79, AT_T19_80 and AT_T19_81 (Figure 4.8 c)) all had minor variations in active mass and OCVs. Both sets of cells, from AT_T22 and AT_T19, had discrepancies between the three parallel cells that were fabricated. Cell AT_T22_75 had the highest amount of active mass, the lowest OCV and did not experience the capacity increase as for the other cells, while cell AT_T19_79 had the highest OCV and performed worse than cell AT_T19_81 with the lowest OCV. The capacity increase around cycle number 50 is still observed for different graphite samples. All of the cells presented in Figure 4.8 were cycled under the same conditions as the cells from electrode sheet AT_T17. We see that cells fabricated with electrodes using different graphite samples behave similarly.

All the previously fabricated cells still had a significant loss of capacity when compared to commercial cells utilizing graphite. After discussing with colleagues in our group and

MoZEES partners, we decided to change the lower cut off voltage 0.01 V to 0.005 V to see if this would improve the cycling stability. Six cells from the same electrode sheet were fabricated, and three of these cells were cycled at voltage window 0.005-2.0 V vs Li/Li^+ and the other three were cycled at voltage window 0.01-2.00 V vs Li/Li^+. Figure 4.9 shows the cells cycled at voltage window 0.005-2.0 V vs Li/Li^+, while Figure 9.1 in Appendix, shows the cells cycled at voltage window 0.01-2.0 V vs Li/Li^+. Aside from the new voltage window, the other settings in the cycling program remained the same. These six cells were cycled with a current density of 50 mAh g^{-1}. We used electrolyte E2 for all the cells, cells cycled at voltage window 0.005-2.0 V vs Li/Li^+ and 0.01-2.0 V vs Li/Li^+, and the main difference between electrolyte E1 and E2 is that the latter has an additional additive, FEC 10 wt%.

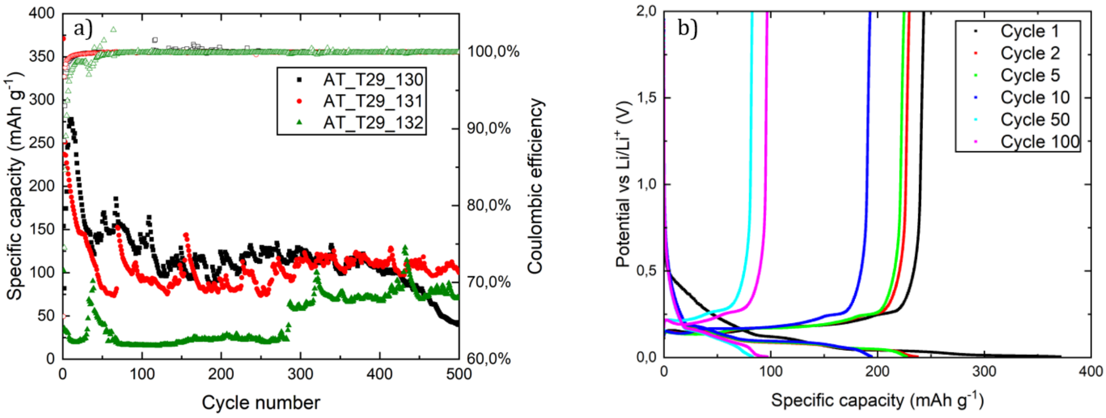

Figure 4.9: a) comparison of GC measurements for cells AT_T29_130, AT_T29_131 and AT_T29_132 displaying the change in specific capacity against cycle number and coulombic efficiency is displayed at the top of the figure. b) shows a representative GC plot for cell AT_T29_131. Electrolyte E2 was used in cell fabrication and voltage window 0.005-2.0 V vs Li/Li^+ was used for the GC measurements.

Cells AT_T29_130, AT_T29_131 and AT_T29_132 had OCVs of 2.29 V, 2.82 V and 2.88 V. The cell with both the highest amount of active mass and OCV performed the worst of the three cells. Here, we also see that irregular cycling occurs which is completely different from previous tests. Multiple capacity increases occur over the 500 cycles. The overall specific capacity at the end of the cycling program is higher than what we observed for other cells and these cells also managed to retain their specific capacity better over the 500 cycles, with the exception of the irregular cycling. Slurry production and cell fabrication remained the same, only the lower voltage and the addition of FEC in the electrolyte changed.

We also performed GC measurements on graphite sample G4 as this sample had a noticeable difference in particle morphology. The MoZEES partner, who we acquired the graphite samples from, informed us that sample G4 had smaller domain than sample G3, but did not specify the size of the domains. They also mentioned that the size of the domains would affect electrochemical cycling performance. Electrode sheet AT_T20 (graphite sample G4) was made with the same procedure as electrode sheets AT_T17, AT_T22 and AT_T19. These cells had electrolyte E1 and the GC data for cells fabricated from electrode sheet AT_T20 is shown in Figure 4.10.

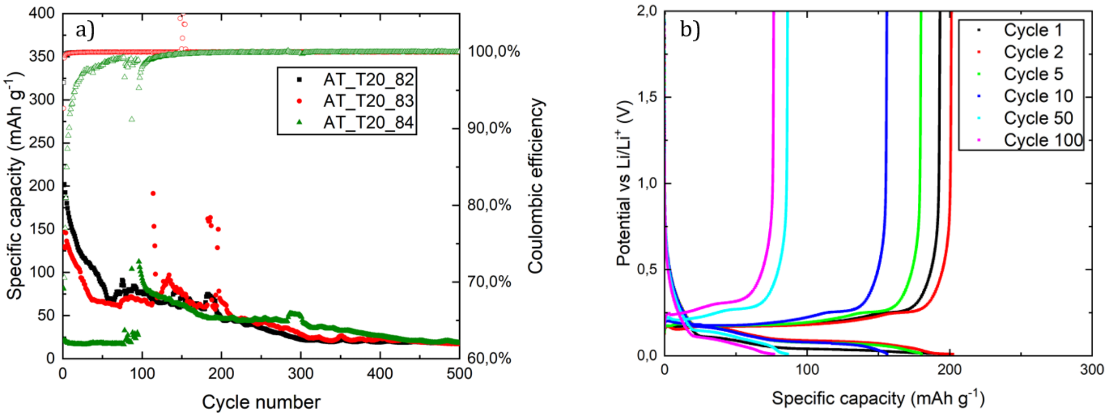

Figure 4.10: a) comparison of GC measurements for cells AT_T20_82, AT_T20_83 and AT_T20_84 displaying the change in specific capacity against cycle number and coulombic efficiency is displayed at the top of the figure. b) shows a representative GC plot for cell AT_T20_82. Electrolyte E1 was used in cell fabrication and voltage window 0.01-2.0 V vs Li/Li$^+$ was used for the GC measurements.

These cells were cycled with the GC program that most cells were cycled with, current density of 50 mAh g^{-1} and voltage window 0.01-2.0 V. There is discrepancy between cells AT_T20_82, AT_T20_83 and AT_T20_84, irregular cycling occurs for these cells where the capacity suddenly increases randomly at different cycle numbers. The most noticeable change in these cells is that the sudden large specific capacity increase we noticed for previous cells has been replaced by another behavior that increases specific capacity.

4.4 *Operando* XRD

To obtain an insight into the phase evolution and the structural changes in graphite during lithiation and delithiation, we have performed a series of *operando* XRD measurements. To make sure that the conclusions regarding the cycling mechanism are not specific for one particular type of graphite, the measurements were done on a variety of graphite samples such as uncycled, cycled, synthetic, natural and produced by different manufacturers. These are all factors that could influence both the performance and the phase transitions of graphite during cycling. The following section demonstrates a selection of *operando* measurements performed at RECX laboratory at UiO and ESRF. The measurements were conducted using the special electrochemical cell designed for performing *operando* XRD experiments in transmission mode as pictured in Figure 3.2 in Subsection 3.4.2.

4.4.1 *Operando* XRD uncycled graphite

We first measured uncycled G1 in the *operando* XRD setup using a half-cell setup similar to a coin cell. The measurements were conducted using RECX instrumentation at UiO. The *operando* XRD measurement and electrochemistry are seen in Figure 4.11, where the operando measurement is represented as a 2D map. Each scan through the Q range represents an individual XRD pattern and corresponds to a point on the charge/discharge curve (shown on the right side). Here, the transition of the graphite 002 peak (at 1.87 Å^{-1}) into 001 LiC_6 (at 1.70 Å^{-1}) and back is shown. This peak corresponds to the spacing between graphene layers and therefore, most of the previous works were particularly focused on examination of evolution of this peak[38, 40].

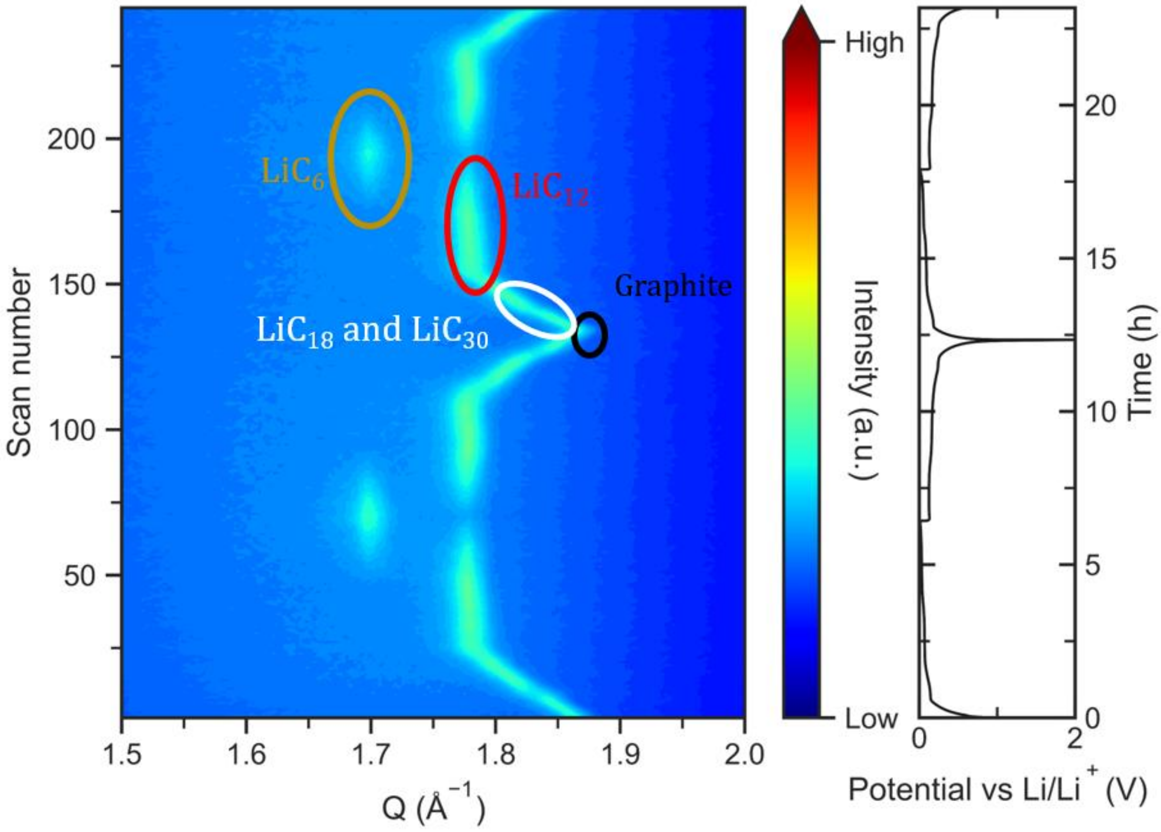

Figure 4.11: The evolution of 002 reflection for graphite sample G1 during galvanostatic cycling (electrochemistry is shown on the right panel of the figure). Graphite (black circle), LiC_{18} and LiC_{30} (white circle), LiC_{12} (red circle) and LiC_6 (gold circle.)

This cell was fabricated with an electrode from electrode sheet AT_T1 that was made using the in-house procedure. The following ratios 3 wt% CMC, 2wt% CB and 95 wt% graphite were used to weigh out 1 g total of solid materials and 1.5 g distilled water was the total solvent added. Casting thickness for this electrode sheet was set to 500 µm thickness after calendaring was 120 µm. The cell did not undergo any electrochemical cycling prior to this measurement and therefore Figure 4.11 illustrates the first two cycles for the newly fabricated cell cycled at C-rate to C/6. The left-hand side of the figure shows the 2D map of all the collected X-ray diffractograms combined to a single figure. The transition from graphite (1.87 $Å^{-1}$ black circle) to LiC_6 (1.70 $Å^{-1}$ gold circle) during lithiation is clearly seen. However, this transition occurs through the formation of other intermediate phases. Based on the previous studies, those could be identified as LiC_{12} (1.79 $Å^{-1}$ red circle), LiC_{18} (1.82 $Å^{-1}$ blue circle) and LiC_{30} (blue circle), which has its peak close to LiC_{18} due to overlap. The identification of LiC_{30} phase differs in the literature, resulting in either LiC_{30} or LiC_{36}[38, 50]. As a result of lithiation, the structure has a gradual increase in the interlayer distance, z-direction, from graphite (3.37 Å) towards LiC_{12} (3.516 Å), through LiC_{30} (3.469 Å) and LiC_{18} (3.515 Å) and suddenly jumps in value when LiC_6 (3.703 Å) forms. This first XRD *operando* measurement shows that sample G1 is able to transition from graphite to LiC_6 and back, and also that the LiC_6 "island" located at 1.7 $Å^{-1}$ slightly decreased in intensity from the first to second cycle. Figure 4.12 shows the other reflections from the same measurement (Figure 4.11) and the Cu-foil and Li-metal reflections are also present.

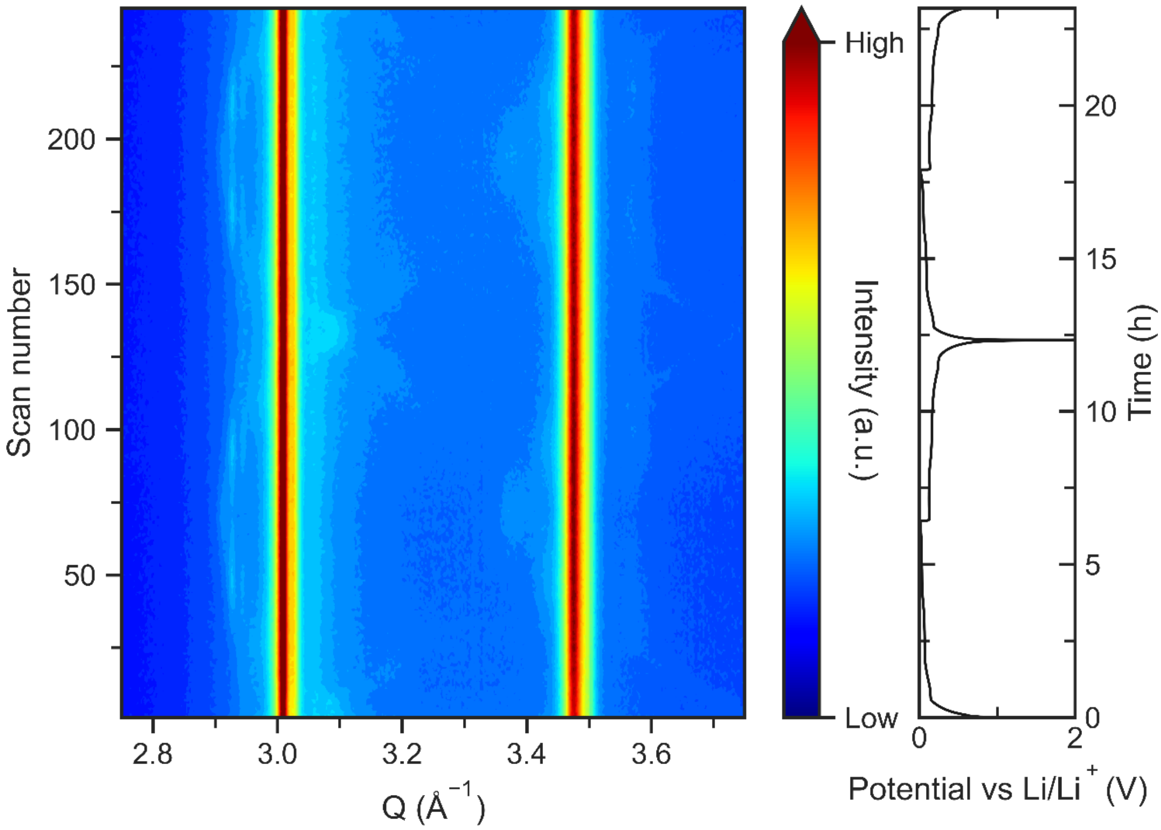

Figure 4.12: The evolution of 100 (2.87 $Å^{-1}$), 101 (3.01 $Å^{-1}$), 102 (3.34 $Å^{-1}$) and 004 (3.64 $Å^{-1}$) reflections of graphite sample G1 during galvanostatic cycling with a C-rate of C/6 (electrochemistry is shown on the right panel of the figure).

As the information available in XRD patterns is not limited to a single 002 reflection, we have decided to look at the other reflections as they provide additional information of the changes graphite undergoes during lithiation and delitiation. As mentioned earlier, most papers that explore this mechanism in graphite usually do peak fitting with the 002 graphite peak and disregard the other low intensity graphite peaks with *hkl* indices 004 (3.75 $Å^{-1}$), 102 (3.45 $Å^{-1}$), 101 (3.09 $Å^{-1}$) and 100 (2.95 $Å^{-1}$). Similar to the main graphite reflection, these indices also change when graphite transitions through the different stages, thus containing information about the structural changes beyond just expansion of distance between graphene layers. This will be discussed in detail in Section 5.3.

4.4.2 *Operando* XRD cycled graphite

Another point of interest was to see how the lithiation and delithiation process vary as cycling of graphite continues, i.e. is the cycling mechanism different at the start and at the end of the anode lifetime. This is important to understand the structural changes associated with the degradation (or change of operating mechanism), so that adequate treatment can be applied in order to recycle the material. For this purpose, cell AT_T17_67, which had gone through 500 cycles (Figure 4.7 a) and b) in Section 4.3), was fabricated into the *operando* cell with a fresh Li-metal disc and more electrolyte, then cycled. The collected diffractograms and corresponding electrochemistry can be seen in Figure 4.13.

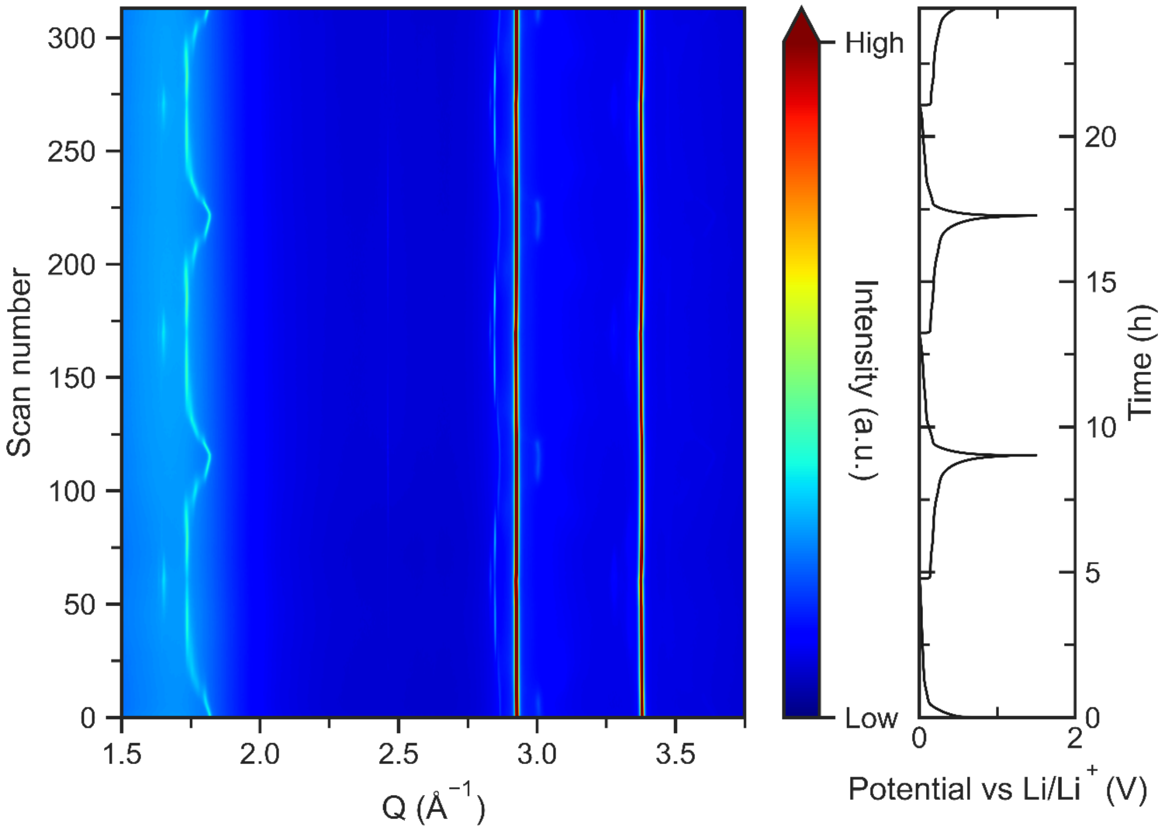

Figure 4.13: The evolution of 002 (1.83 Å^{-1}), 100 (2.87 Å^{-1}), 101 (3.01 Å^{-1}), 102 (3.34 Å^{-1}) and 004 (3.64 Å^{-1}) reflections of graphite sample G1, which underwent 500 galvanostatic cycles in a coin cell, during galvanostatic cycling with a C-rate of C/6, during galvanostatic cycling (electrochemistry is shown on the right panel of the figure).

For this measurement, the same current density (50 mAh g^{-1}) was applied as for the cycling of the coin cell and most parameters were similar aside from the different electrolyte that was used (here E2). The figure shows that the transition from graphite to LiC_6 and back still occurs despite the electrode cycling for many cycles. Figure 4.7 a) and b) in Section 4.3 showed that the electrode had lost most of its initial capacity, but in the *operando* measurement the cell manages to reach a capacity of 251 mAh g^{-1}, which is close to the initial capacity of 303 mAh g^{-1} the electrode had in the coin cell, indicating that the electrochemical performance is restored when the electrolyte is refilled and a new Li metal foil is added.

4.4.3 High resolution *operando* XRD

The following set of measurements were performed at the ESRF to get more detailed information from the *operando* XRD measurements. Specifically, rapid acquisition allows to collect data with high time resolution allowing to properly define all phase transitions occurring in graphite during lithiation and delithiation. Figure 4.14 shows the diffractograms and electrochemistry for sample G1 with C/20.

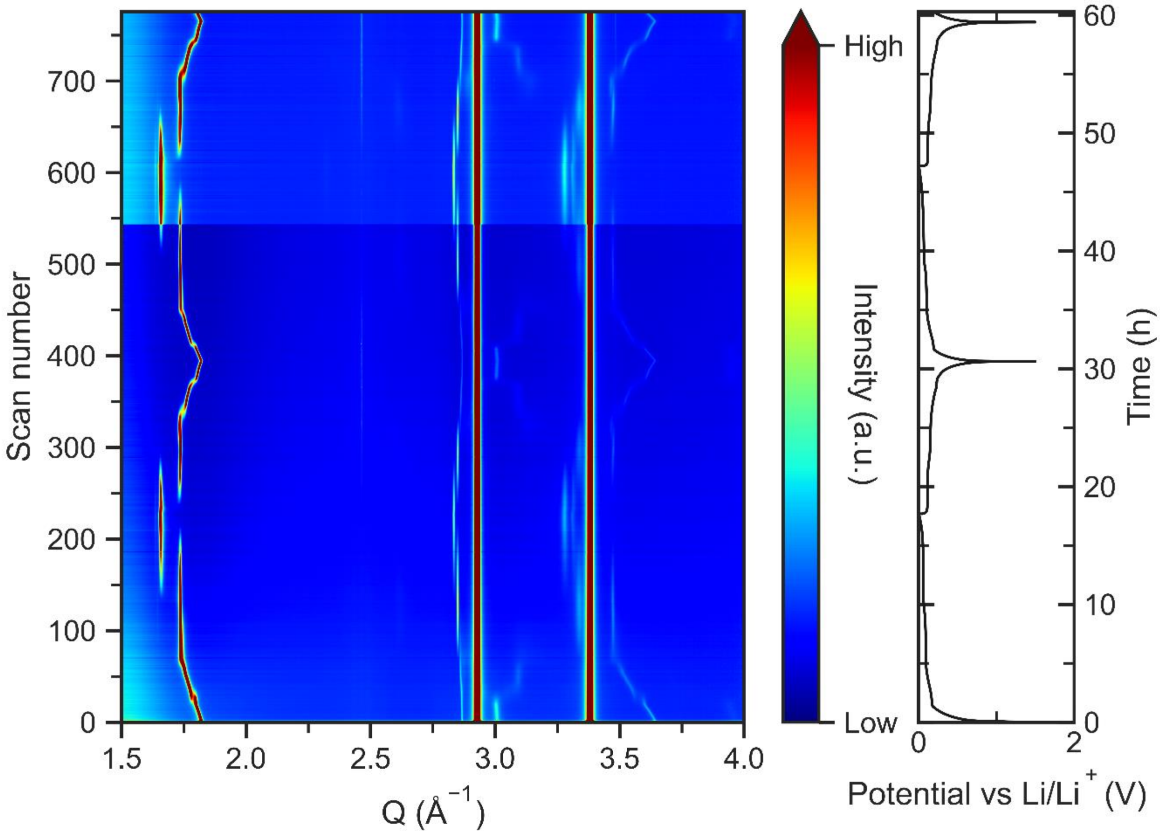

Figure 4.14: The evolution of 002 (1.83 Å^{-1}), 100 (2.87 Å^{-1}), 101 (3.01 Å^{-1}), 102 (3.34 Å^{-1}) and 004 (3.64 Å^{-1}) reflections of graphite sample G1 during galvanostatic cycling with a rate of C/20 (electrochemistry is shown on the right panel of the figure).

We stopped the cell after it had completed two full cycles. Interestingly, a clear mismatch between mechanisms of discharge and charge was observed. Here, the first discharge takes approximately 17.5 hours, which is close to the intended C/20, while the first charge takes approximately 13 hours. Similarly, the second discharge is longer than the second charge. For this sample, transition from graphite to LiC_6 is apparent in the diffractogram (as evidenced by the shift of the 002 peak from 1.83 $Å^{-1}$ to 1.67 $Å^{-1}$). We could more clearly see the differences between phases during intercalation and deintercalation due to the higher intensity and resolution compared to the conventional X-ray diffractometer.

As mentioned above, the operating mechanism of graphite may depend on the lifetime of the sample (i.e. how many cycles the sample went through prior to analysis). Therefore, the next step was to see whether the observed structural changes would change depending on what graphite was used. Therefore, several samples of graphite-based electrodes were acquired from MoZEES partners. These samples were cut from fresh commercial pouch cells and the same type of cells that had undergone a few hundreds of electrochemical cycles. We first assembled the fresh electrodes from the commercial pouch cell into *operando* cells and cycled at a C-rate of C/20, similar to the measurement described above. The diffractograms and the electrochemistry for the electrode which has been exposed to prior cycling can be seen in Figure 4.15.

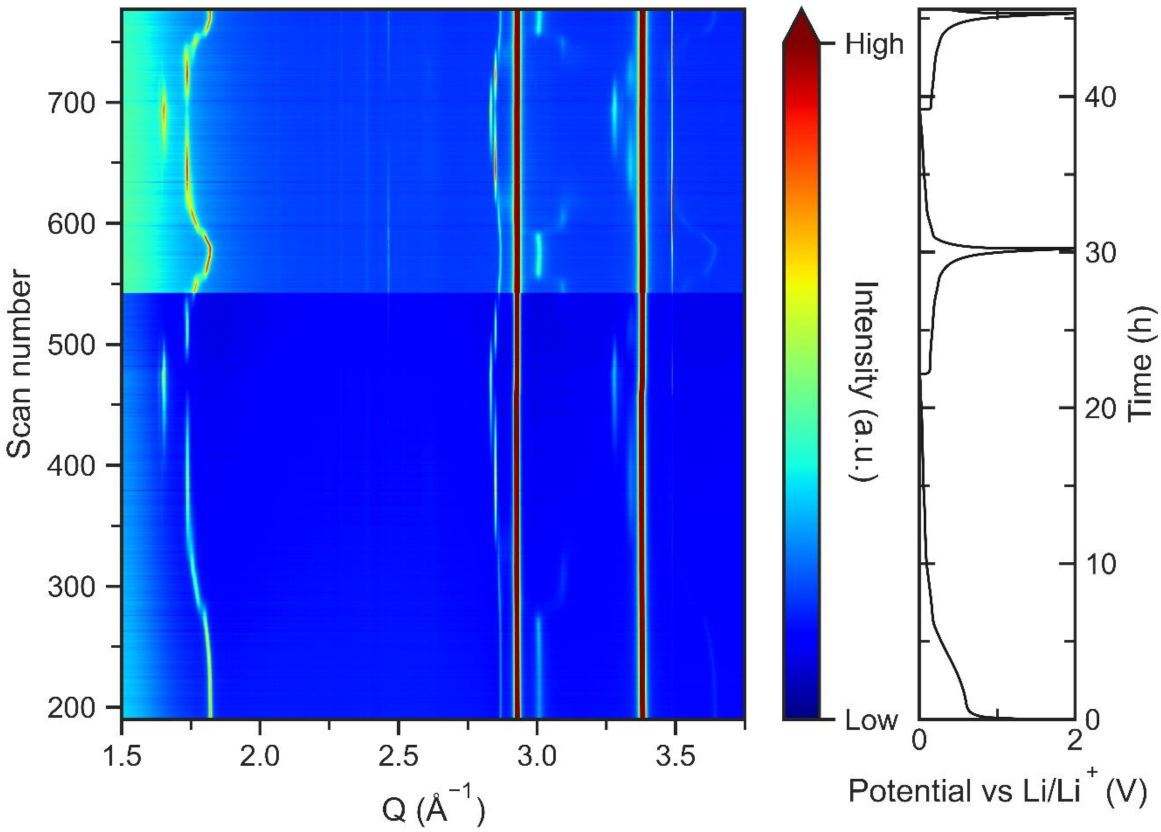

Figure 4.15: The evolution of 002 (1.83 Å^{-1}), 100 (2.87 Å^{-1}), 101 (3.01 Å^{-1}), 102 (3.34 Å^{-1}) and 004 (3.64 Å^{-1}) reflections of graphite electrode cut from a pouch cell, that underwent a few characterization cycles, during galvanostatic cycling with a rate of C/20 (electrochemistry is shown on the right panel of the figure).

The cell completed two full cycles before it was stopped and shows a clear transition from graphite (1.83 Å) to LiC_6 (1.67 Å^{-1}) and back. All the phases, for both the main- and other reflections, are well defined similar to previous measurements. This shows that the same structural changes occur for different graphite samples.

Till now we had mostly tested uncycled pristine graphite, one sample that had undergone 500 electrochemical cycles (Figure 4.7 a) and b) in Section 4.3) and a sample cut commercial pouch cell that underwent a few characterization cycles prior to *operando* measurements. Therefore, we wanted to see if long term cycling of graphite had an effect on cycling mechanism or not. We did an *operando* measurement on an electrode cut from a pouch cell that had cycled approximately 1100 cycles. The measurements were done at a C-rate of C/6 and is shown in Figure 4.16.

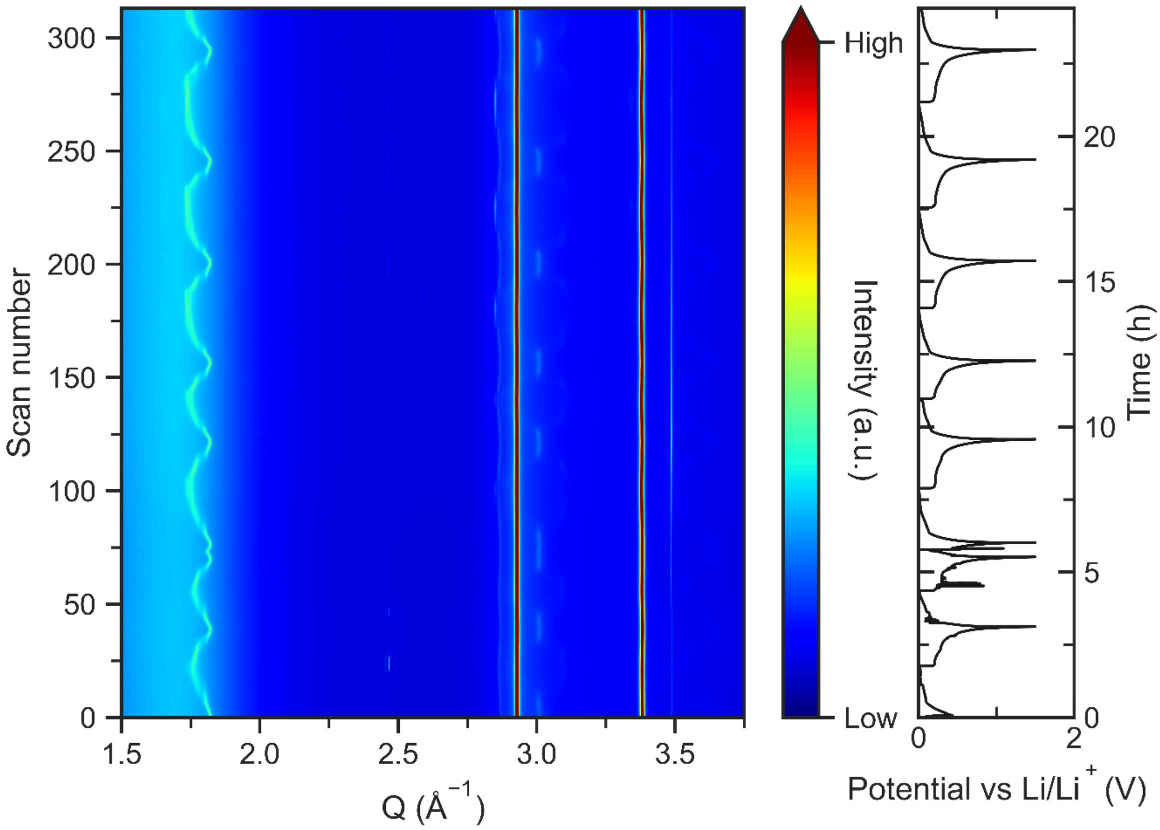

Figure 4.16: The evolution of 002 (1.83 Å^{-1}), 100 (2.87 Å^{-1}), 101 (3.01 Å^{-1}), 102 (3.34 Å^{-1}) and 004 (3.64 Å^{-1}) reflections of graphite from cycled pouch cell (1100 cycles) during galvanostatic cycling with a rate of C/6 (electrochemistry is shown on the right panel of the figure).

Here we see that the sample is not able to fully lithiate graphite to expected LiC_6. Instead, lithiation conducted at this rate stops at LiC_{12} and no phases with higher Li concentration has been detected. We also observed that the cycles become longer as the sample is cycled consecutively. The other reflections are still present in the diffractogram and follow the trend as the main 002 reflection.

Thus, we had tested different types of graphite from different manufacturers in order to see if the data acquired would differ or not and we tested “aged” samples to see any apparent change in the cycling mechanism. The acquired results showed that what we saw for the initial measurement done with sample G1 was not specific to just this sample but occurred in other graphite samples as well and we also noticed that long term cycling had an effect on the cycling mechanism. The next question we had was how the mechanism would change when an even higher C-rate was used. For that purpose, higher C-rates were chosen as C/20 and C/6 showed complete transition from graphite to LiC_6 and back, with the exception on the measurement seen above in Figure 4.16. The fast data acquisition at ESRF allows to perform such measurements with the required resolution. Thus, graphite sample G1 was cycled at a C-rate of C/2 and the measured diffractograms and electrochemistry can be viewed in Figure 4.17.

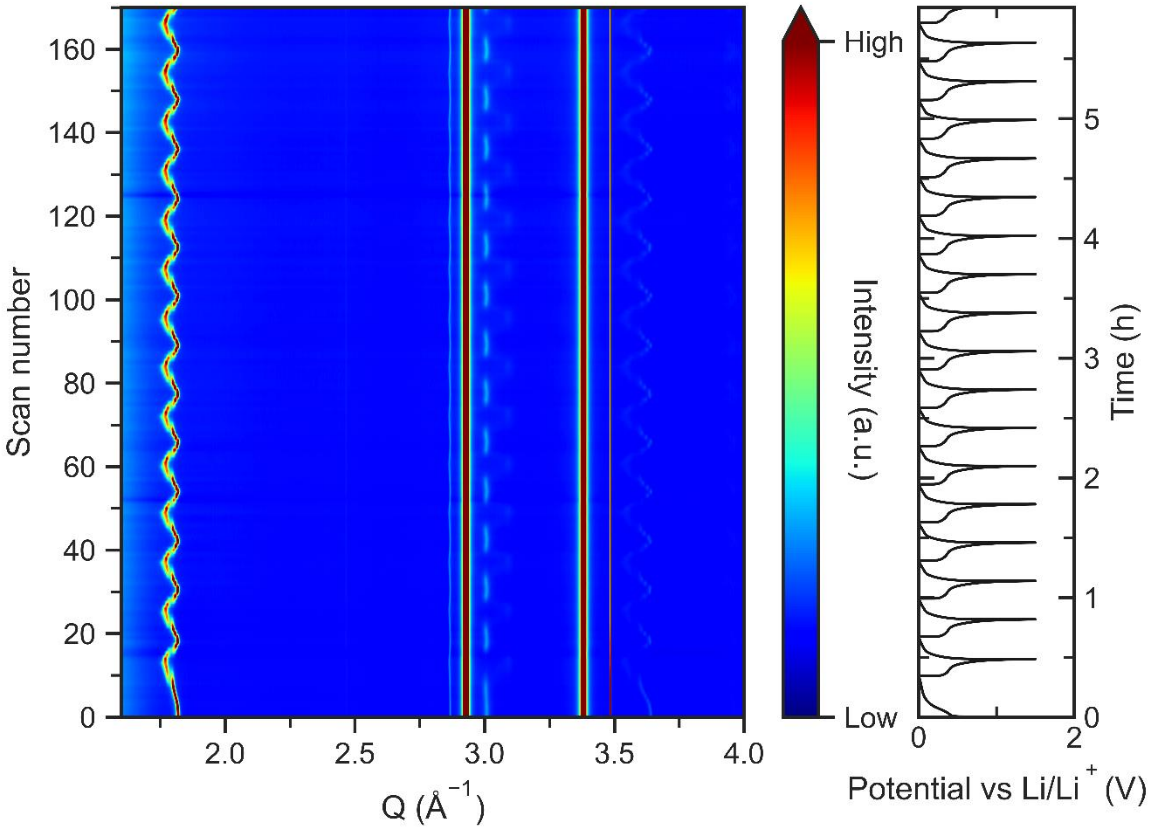

Figure 4.17 The evolution of 002 (1.83 Å^{-1}), 100 (2.87 Å^{-1}), 101 (3.01 Å^{-1}), 102 (3.34 Å^{-1}) and 004 (3.64 Å^{-1}) reflections of graphite sample G1 during galvanostatic cycling with a rate of C/2 (electrochemistry is shown on the right panel of the figure).

The cell completed almost 18 cycles before it was stopped. The diffractogram reveals that the higher C-rate prevents graphite from transitioning to LiC_6, and rather enforces transitions between graphite (1.81 Å^{-1}) to LiC_{12} (1.77 Å^{-1}). Interestingly, the transition to graphite is complete, and no lithiated phases could be observed at high delithiation rates. The other reflections are still apparent despite the faster cycling and lack of transitioning into LiC_6.

Throughout this section, multiple *operando* XRD measurements were shown for different graphite samples. Here we saw the clear transition from graphite to LiC_6, evolution of the 002 reflection of graphite into 001 reflection of fully lithiated phase, and back for multiple samples such as uncycled- and cycled graphite we acquired from MoZEES partners. In addition to the main 002 graphite peak that many are focused on, the evolution of reflections 004, 102, 101 and 100 were shown for all the graphite samples presented. That allows to observe a magnitude of the structural changes occuring in graphite during cycling. Here, it also became apparent that the cycling speed affects the materials ability to transition from graphite to LiC_6. Faster cycling speed prevented graphite from transitioning to LiC_6 and rather ended up with LiC_{12} as the endpoint before transitioning back.

4.5 PDF measurement

With the *operando* XRD measurements, we were able to monitor the phase evolutions in multiple graphite samples and witness the expansion of interlayer distances and other structural changes that occurred during litiation and delithiation. The evolution of the reflections other than 002 clearly indicates that structural changes in graphite go beyond just the expansion in the z-direction. Thus, it is interesting to observe whether the graphene layers contract and expand during cycling. One of the promising techniques to evaluate these changes is pair distribution function (PDF) – using this technique it is possible to observe localized structural changes and thus get the information on C-C distances in graphene layers. Graphene layers are constructed of multiple hexagonal carbon rings and the three different C-C distances in a hexagonal carbon ring is 1.41 Å, 2.47 Å and 2.85 Å. A hexagonal carbon ring in pristine graphite is shown in Figure 4.18.

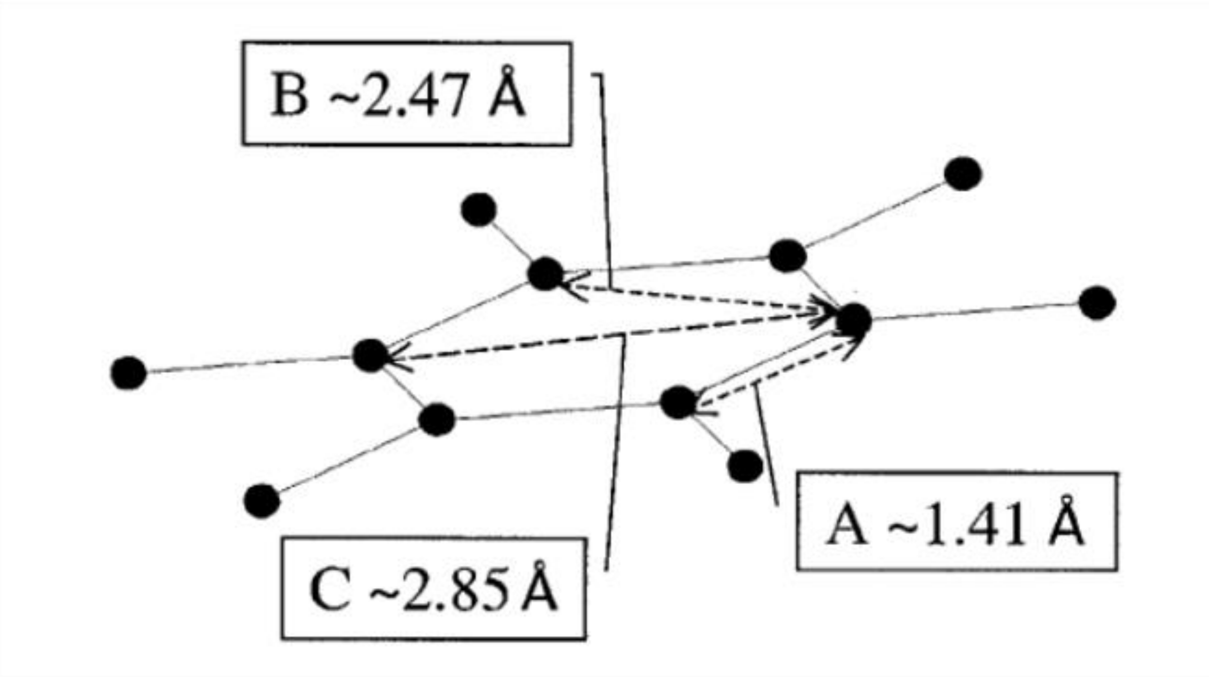

Figure 4.18: Hexagonal carbon ring in pristine graphite with C-C distances 1.41 Å, 2.47 Å and 2.85 Å. Adapted from [51].

Thus, we explored this phenomenon with *ex situ* PDF measurements. Multiple graphite-based electrodes were placed into conventional coin cells using electrolyte E1 and Li metal foil as counter electrode. The cells were cycled at a C-rate of C/6 and the cycling was stopped at different areas between phases LiC_{30} and LiC_{12} during lithiation and delitiation as these are the intermediate phases that are not fully explained. We analysed the *operando* XRD diffractogram (Figure 4.14 in Subsection 4.4.3) and picked measurement points that showed phase transitions. Pristine graphite was also measured as a reference to get correct peak positions during data treatment. During the first lithiation, seven samples were collected. The first sample was stopped 30 minutes from the start of the first lithiation, and the last sample was stopped 5 hours after the first lithiation had started. All PDF measurements for the lithiated samples are plotted together in Figure 4.19.

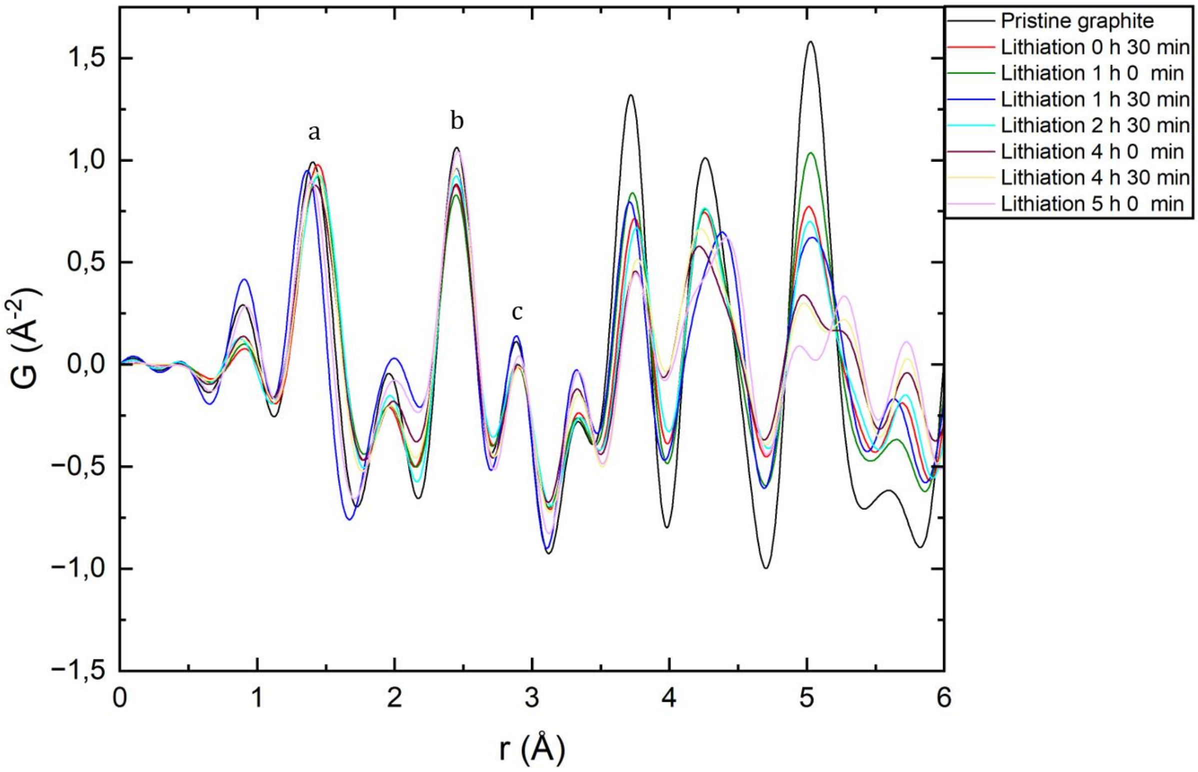

Figure 4.19: PDF pattern for pristine graphite and 7 samples that were collected during the first lithiation.

We decided to have an upper limit of 6 Å on the x-axis as we mainly wanted to observe the change in C-C distance in hexagonal carbon rings and close interactions. In this plot, we see three peaks located at 1.41 å, 2.47 Å and 2.85 Å that correspond to the different C-C distances in a hexagonal carbon ring in pristine graphite. During discharge, these three peaks shift in position, indicating that the C-C distance in the hexagonal rings are changing.

During the first delithiation, 5 samples were collected. The first sample was stopped 4 hours and 30 minutes from the start of the first delithiation, and the last sample was stopped 5 hours and 18 minutes after the first delithiation had started. These are shown in Figure 4.20. Similar to the measurement above, these 5 cells were also cycled at C/6.

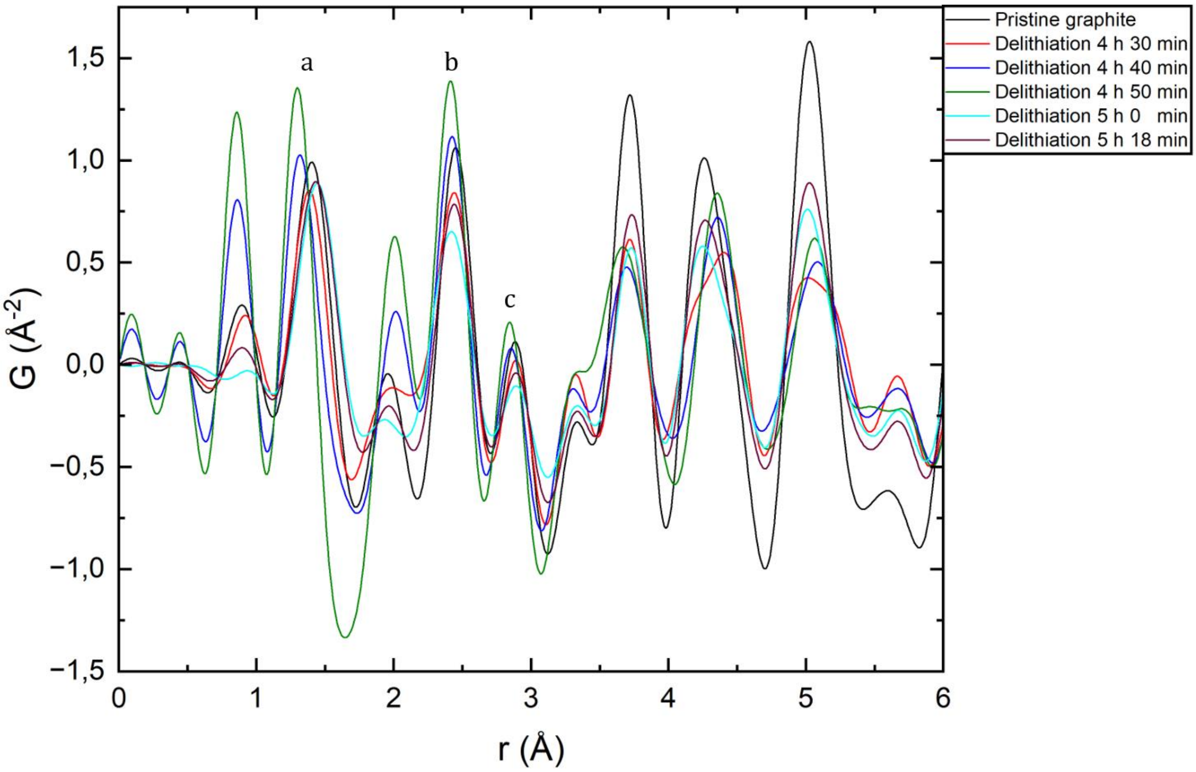

Figure 4.20: PDF pattern for pristine graphite and 5 samples that were collected during the first delithiation.

These cells were stopped mostly in the later part of the delithiation step as the *operando* measurement (Figure 4.14 in Subsection 4.4.3) showed clear phase transitions at these areas. We also see here that the three peaks located at 1.41 å, 2.47 Å and 2.85 Å have a shift in peak position during charge, which shows that the C-C distances in the graphene layer changes during delithiation.

5. Discussion

The following section discusses the results presented above in view of the other considerations published in the literature. This section is split in two part, where optimization of electrochemical performance is discussed first, following a discussion on the structural changes, which graphite undergoes during lithiation and delithiation.

5.1 Optimization of electrochemical performance

As mentioned above, graphite has been extensively studied during the past decades as a battery material. It is the most used anode material in LIBs, due to its cyclability and performance characteristics. Therefore, we thought that it would be a simple task to optimize graphite-based electrodes in coin cells and obtain results somewhat close to that of commercial cells. The standard cycling of commercial cells involves losses of initial capacity during formation cycling and then a stable capacity over thousands of cycles. However, obtaining such performance behavior proved to be more difficult than expected. It should be noted, that the reason for obtaining cells with a long cycle life is to obtain a sample of cycled ("used") graphite and compare lithiation and delithiation mechanisms at different stages of material lifetime. The prior information we had on the different graphite samples was that G1, G2, and G4 are samples of synthetic graphite, while G3 is a natural graphite sample. These samples also underwent different sets of surface treatments. In addition, Samples G3 and G4 have varying domain sizes, where G3 has larger domains than G4. Through XRD analysis, we confirmed that all the samples contained only graphite and SEM showed that the samples have varying morphologies. Thus, it would be reasonable to assume that from such a variety of samples it should be possible to create long-lasting electrodes with reasonable capacity.

We noticed that there were a number of discrepancies for cells fabricated from the same electrode sheet and this occurred for all graphite samples. Those could be shortly summarized as follows:

1. There were minor variations in active mass (at most 0.1-0.7 mg) for three cells that were fabricated, and this is not a significant difference considering the high active mass all the electrodes have (14.6-16.7 mg).
2. Multiple cells had worse electrochemical performance than cells with lower OCVs.

3. When a set of three cells were fabricated, all coin cell parts were lined up making three cells from left to right. Sometimes, the cell that was built fist had the worst electrochemical performance, while other times it was the second or the third

These discrepancies in electrochemical performance appeared in somewhat random fashion.

For cells fabricated from electrode sheet AT_T17, containing sample G1, we noticed that a sudden large capacity increase had appeared (Figure 4.7 Section 4.3). That phenomena was not observed for the previous cells. This increase occurred in the same area for all three cells, around cycle 50 after the initial loss of specific capacity and a significant portion of the lost specific capacity was restored. This increase was also noticed for cells fabricated with electrodes containing sample G2 and G3. These specific capacity increases have minor differences but similar behavior. It is worth noting that electrode sheets AT_T17 (sample G1), AT_T22 (sample G2) and AT_T19 (sample G3) were all made using the same procedure and the cell fabrication was also similar for all the cells. The SEM images show that sample G1 and G2 have similar particle morphology, with variations in size from what we could see in the SEM images. Sample G3 has different particle morphology than sample G1 and G2. Despite the differences in morphology, synthetic samples G1 and G2 behave similarly to natural graphite sample G3 during GC measurements. The observed capacity increase for samples G1, G2 and G3 piqued our interest as our partners in FEM center MoZEES had not previously experienced this. An unusual behavior of graphite-based electrodes have been reported in one publication that explored the occurrence of capacity increases at early cycles for commercial NMC/graphite LIBs [52]. In this paper, Guo *et al*. noticed two different types of capacity increases that occurred during two different voltage windows 0.001-1.0 V and 0.001-0.2 V. The first type of capacity increase was a gradual increase over a few cycles and the second type of capacity increase was a stepwise increase over 20 cycles. We cycled our cells at a different voltage window, 0.01-2.0 V vs Li/Li^+, and we had a single large capacity increase that was different from what Guo *et al*. observed. The authors explained that the capacity increase occurred as the interlayer distance in graphite could not fully recover during delithiation. The resulting enlarged interlayer distance reduces insertion resistance of Li-ions, thus increasing Li-ion diffusion rate. However, such explanation does not seem to be applicable in the present work as it would rather explain better rate capability for the material rather than capacity increase. The authors also mentioned that cracks and partial exfoliation would occur during cycling, and this would expose more electrode surface to the electrolyte that would increase the amount of graphite that can intercalate Li-ions and this would result in capacity increase. One possible explanation for unusual capacity is a restructuring of the electrodes during cycling, where material previously blocked from participating in the electrochemical activity becomes available. That is essentially related to the methods of electrode preparation. Our cells had initial capacities that were lower than the theoretical capacity of 372 mA h g^{-1} [14], and the electrodes were thick (86.9-120.0 μm) and had high amounts of active mass (14.6-16.7 mg). As a result, the cell most likely did not utilize the whole material. During cycling, more of the material was activated resulting in capacity increase.

The capacity loss still represented an issue, which could not be improved despite making changes in slurry process, coating and calendaring. After discussing with multiple MoZEES partners, we were recommended to explore a different voltage window with a lower cut off voltage, 0.005-2.0 V Li/Li^+. Electrode sheet AT_T29 was made the same way as AT_T17 and they both contained graphite sample G1. We fabricated six cells to test three cells at two different voltage windows, 0.005-2.0 V Li/Li^+ and 0.01-2.0 V Li/Li^+. These cells had similar electrochemical behavior to each other and changing the voltage window had no significant effect. However, all cells fabricated from electrode sheet AT_T29 (Figure 4.9 Section 4.3 and Figure 9.1 Appendix), using electrolyte E2, behaved drastically different from the cells fabricated from electrode sheet AT_T17, which used electrolyte E1. The only difference between electrolytes E1 and E2 being 10wt% FEC in E2. As a result, a single large capacity increase observed for cells fabricated from electrode sheets AT_T17 (G1) was replaced with multiple capacity increases over the course of 500 cycles. Cells from electrode sheet AT_29 also managed to retain a specific capacity of around 100 mAh g^{-1} due to a gradual increase over many cycles. The addition of FEC had altered the electrochemical cycling of graphite sample G1. Etacheri *et al*. tested different electrolyte compositions to see the effect of FEC on electrochemical cycling of Si nanowires [53]. Similar to us, Etacheri *et al*, used two electrolytes, among others, where the electrolyte composition was similar with the exception of one electrolyte containing FEC, while the other electrolyte did not. The authors noticed that electrochemical performance was enhanced for cells containing

FEC and stable reversible capacities over prolonged cycling. They explained that the increased performance was due to superior properties of the SEI layer formed during electrochemical cycling. Such SEI layers formed in cells using FEC-containing electrolytes are thin and led to lower overpotential and impedance for the lithiation and delithiation process in contrast to cells using an electrolyte without FEC.

The irregular cycling observed for cells from AT_T29 could also be the result of the electrode sheet itself. According to the electrochemical data, cell AT_T17_67 had almost no capacity left after completing the initial 500 cycle program. The electrode was taken out and fabricated into a new cell with a new Li metal foil and replenished with electrolyte E2 (used electrolyte E1 during initial cycling). We then saw that the cell had higher capacity in the newly fabricated cell, gradual increase of capacity over prolonged cycling (Figure 9.2 in Appendix) and did not experience irregular cycling as the cells from AT_T29 experienced. The increased initial capacity could have been due to surface "refreshment", delamination of electrode surface when it was removed from the separator, which gave a similar effect as the large capacity increase we noticed for cells from electrode sheets AT_T17, AT_T22 and AT_T19. We also noticed that the graphite electrode consumed large amounts of electrolyte as it had a substantial mass increase, and the cell environment was dry. This could also have been a potential reason for the poor electrochemical performance.

Cells fabricated from electrode sheets AT_20 contain synthetic graphite sample G4. Cells from this sample are also plagued with discrepancies as seen for other sets of cells. The particle morphology of sample G4 differs substantially from the other three graphite samples as it has a high occurrence of graphite flakes. We were also informed by our MoZEES partners that sample G4 has smaller domains than sample G3 and the domain size would affect the electrochemical performance of the sample. Persson *et al.* studied lithium diffusion in graphitic carbon and showed through experimentation and computation that Li-ion diffusivity is higher in the direction parallel to the graphene planes ($\sim 10^{-6}$ cm^2 s^{-1}), as compared to the Li-ion transport along grain boundaries ($\sim 10^{-11}$ cm^2 s^{-1}) [54]. They concluded that Li-ion diffusivity in any graphitic carbon will depend critically on the size of the graphite domains as well as the orientation of the graphite domains with regard to the intercalative/deintercalative flux. Graphite particles with large and aligned domains will therefore perform better in batteries as the

Li-ions will spend more time diffusing along planes where it has higher diffusivity, compared to graphite samples where the domains are smaller and misaligned as the Li-ions will spend more time diffusing along grain boundaries. Regarding performance, we do see that samples G4 behaves differently than G3, by having lower starting specific capacities overall when looking at cycles 1-100.

All cells fabricated from different graphite samples had poor electrochemical performance in the coin cells as they struggled to retain capacity over multiple cycles. We here observed a large capacity increase during cycling, that was not reported previously. Changing the voltage window from 0.01-2.0 V Li/Li$^+$ to 0.005-2.0 V Li/Li$^+$ did not result in a significant change, but the use of electrolyte E2 with FEC resulted in better capacity retention even though irregular cycling was observed.

5.2 *Operando* measurements

Within the present work a series of operando measurements were conducted to gain an understanding of the operating mechanism of graphite and how it changes with prolonged cycling. When comparing the *operando* XRD measurements we did at the RECX laboratory at UiO for uncycled and cycled graphite (Figures 4.11 in Subsection 4.4.1 and 4.13 in Subsection 4.4.2) it becomes evident that there are differences in the cycling mechanism of graphite. The phase evolution of graphite to LiC_6 is still apparent, which is evident from the observed diffraction peaks. Both *operando* measurements were conducted using C-rate of C/6 which corresponds to a current density of 50 mAh g^{-1}. Similar to the capacity increase we noticed for the cycled ("used") electrode that was placed into a new coin cell with a new Li-foil and replenished electrolyte (Figure 9.2 in Appendix), a similar electrode used for the fabrication of the *operando* cell also experienced a capacity increase. The capacity increase is most likely of the same reason as mentioned above.

The measurements performed at ESRF were deliberately conducted using multiple samples of graphite and at various cycling rated. Thus, we were able to confirm that the mechanism we observed for sample G1 was not exclusive to one type of graphite. The mechanism of phase evolution also occurred for different graphite samples. This became evident as we were able to observe the evolution of the reflections corresponding to graphite peaks to LiC_6 peaks and back. The other intermediate stages between graphite and fully lithiated graphite were also present as for sample G1. In addition, we observed that the C-rate had a significant effect on the evolution of the 002 reflection as the samples were lithiated and delithiated. At C-rates of C/20 and C/6, it was possible to fully lithiate graphite to the LiC_6 phase and fully delithiate it back to the original graphite, while with a higher C-rate of C/2, graphite could only transition to LiC_{12} during lithiation. This effect was clearly seen for all other graphite reflection patterns (100, 101, 102 and 004) and not only the 002 reflection which is mainly used in Rietveld and other XRD analysis that has been published [33, 38]. This shows that all reflections correlate to each other and change similarly depending on the phase evolution of the graphite material

The tested samples were not designed for high rate performance, but other graphite samples are. Sun *et al*. tested a full cell with $LiFePO_4$ as cathode and graphite as anode and cycled these cells at C-rates between 1C-50C. In this work, the authors were still able to observe a phase evolution from graphite to LiC_6 and back and maintain a stable specific capacity over hundreds of cycles with respect to the different C-rates used [55]. The full evolution was evident as the voltage plateaus are present signifying the transition to the different stages. This was most probably a carefully optimized cell, and our samples could potentially achieve this too in a full cell with further optimization. A concern with higher C-rate is lithium plating. Finegan *et al*. explored the spatial dynamics of lithiation and lithium plating during high-rate operation of graphite electrodes [56]. The authors showed that favorable conditions for Li plating occur at high C-rates, causing accelerated degradation and safety concerns. The presence of Li plating changed the behavior of the underlying graphite, such as causing co-existence of LiC_6 and graphite in the fully discharged state. Therefore, higher rates must be chosen carefully as to prevent lithium plating and reduced electrochemical performance.

5.3 Structural changes of graphite during intercalation and deintercalation

Previously in Section 2.3, we introduced different models that tried to explain the intercalation and deintercalation mechanism and realized that none of the fully able to explain it due to weaknesses. The Rüdorff-Hofmann model has empty layers, no clustering and flat layers [23], Daumas-Herold model has empty layers and poor explanation of ordered staging [24], localized domains model proposed by Weng *et al.* does not explain ordered staging and requires defect healing [29], and the crystal structures proposed by Missyul *et al*. [38], which is based on the Rüdorff-Hofmann model and well defined crystal structures of graphite and LiC_6, has non related space groups leading to unusual Miller indices. These models by themselves fail to explain the lithiation and delitiation mechanism. However, these models have revealed some of the structural features that are helpful in explaining the lithiation and delithiation mechanism:

1. Formation of Li-ion clusters
2. Graphene layers that are not completely flat
3. Lack of completely unoccupied layers.

In the research community, graphite and LiC_6 are well known phases with well determined bond lengths/angles as they are reasonably well-ordered structures, but there is a lack of information on all the disordered intermediate phases and their transitions (Stages 1L to 4L, 4L to 3L and 3L to 2 L).

using our *operando* XRD data, we are able to observe the evolution of the 002 graphite peak to 001 LiC_6. From this evolution and the inverse relation between peak position and interlayer distance, we observe that the change in interlayer distance in graphite is driven by the Li-ion content in the graphite structure. This change is well documented in previous literature as reviewed in the introductory section. However, these interlayer distances, especially for the intermediate phases between graphite and LiC_6, is not fully descriptive if the fact that graphene layers are not completely flat is taken into the consideration. During lithiation and delithiation, the structure will adopt different interlayer distances throughout the graphite structure depending on the density of Li-ion clusters. It is important to keep in mind that the data presented in research and our own XRD data does not show the actual, local interlayer distance in the structure, but an average in the measured area. Despite it being an average, it still shows that the structure is expanding during lithiation and contracting during delithiation.

In pristine graphite, the van der Waal forces and repulsion between graphite is keeping the individual graphene layers at a distance of 3.35 Å from each other. The pristine graphite structure cannot adopt AA stacking as the distance is too small and the orbitals of the carbon atoms overlap causing repulsion. Here, a C-atom is situated directly above or below the center of this ring in the adjacent B-type layers. As Li-ions intercalate into the structure, the interlayer distance gradually starts to increase (unevenly throughout the structure due to clusters of Li-ions forming) due to the repulsion the Li-ion introduces. Eventually, the layers shift in position from ABAB in graphite to AA in LiC_6 as the repulsion introduced by the Li-ions in the structure increases the interlayer distance minimizing the repulsion between C-atoms in one layer and C-atoms in the layer above or below, as shown in Figure 5.1.

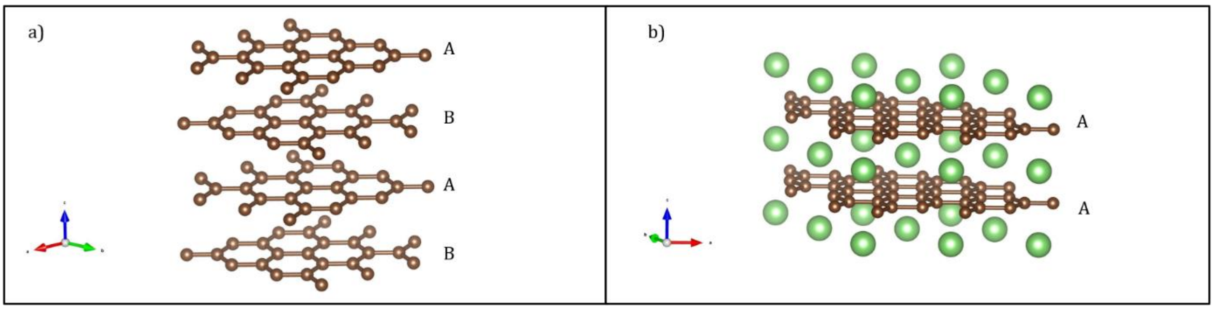

Figure 5.1: Stacking sequence of graphene layers in a) graphite and b) LiC_6.

At this point, Li-ions are situated in the middle of two hexagonal carbon rings between two layers in AA stacking. While in pristine graphite with ABAB stacking, the shifting of layers resulted in carbon atoms in the B layer being in the middle of two hexagonal carbon rings between the two A layers. Li-ions have not substituted C-atoms, but rather moved position from being in the middle of the ring to the edge of the ring where it is situated right in the middle of its adjacent carbon atom in the layers above and below.

The stacking order of graphene layers and interlayer distance proposed in literature becomes unreliable due to the average values the measurements show, when in reality, the intermediate phases are likely disordered and uneven. However, this shift in layer from ABAB stacking in pristine graphite to AA stacking in LiC_6 is something that potentially could be observed in our PDF data as it shows the average local structure rather than the long range-average found in the total structure. For pristine graphite, we see a peak situated at 3.72 Å that could correspond to the distance between any C-atom which sits directly above or below the center of this ring in the adjacent B-type layers (3.64 Å measured from the crystal structure of graphite) and this is not unreasonable when considering that the graphene layers are not completely flat. During lithiation we see that the peak position shifts to both lower and higher positions until it eventually has peak position at 3.76 Å. What we need to keep in mind is that we do not have PDF data on fully lithiated graphite (LiC_6). In LiC_6, interlayer distance is 3.69 Å (measured from the crystal structure of LiC_6). There is also minor variation in our acquired peak positions and those seen in literature [51]. But this could potentially be the shift of layers that is observed. The problem here is that there is another C-C distance in the layer itself that could correspond to this peak. Petkov *et al*. performed PDF on nanoporous carbon and concluded that this peak is another in-plane C-C distance [51]. We have an additional PDF peak located at 3.33 Å (Figure 4.19 and Figure 4.20 in Section 4.5) that could correspond to the interlayer distance. However, this peak does not shift towards 3.69 Å, which is the average interlayer distance in LiC_6 reported.

We also correlate the peak positions in the PDF data to the three different C-C distances present in a hexagonal carbon ring by examining the crystal structure of graphite were also able to correlate the peak position in the PDF data to the three different C-C distances that are present in a hexagonal carbon ring by looking at the crystal structure of graphite. Peak positions at 1.40 Å, 2.45 Å and 2.88 Å correspond to the three C-C bond distances a, b and c in a hexagonal carbon ring (Figure 4.18 in Section 4.5). In our PDF data (Figure 4.19 and Figure 4.20 in Section 4.5), we observe a shift in peak position for all three peaks during lithiation and delithiation. The three peaks shift to lower and higher positions, relative to the positions in pristine graphite, indicating that the C-C distances in hexagonal carbon rings contract and expand during both lithiation and delthiation. As a result, the graphene layers contract and expand during lithiation and delithiation. The change of the three C-C distances in the hexagonal carbon ring is most likely due to Li-ions occupying the center of the rings. Some are occupied, while others are not, and this will change the lengths of the different rings in a layer. In addition, an electron goes into the hexagonal carbon ring, and this electron will be placed in the antibonding orbital weakening the C-C bonds [41]. There is another aspect that could be explained by these changes in distance. The Daumas-Herold model describes Li-ion "island" formations that occurs due to Li-ion clusters between two individual graphene layers that distort the local area. Van der Waals forces attract two layers together, while Li-ion clusters introduce repulsions, and this should bend the layers causing the distances in the hexagonal carbon rings to change since interlayer distance in areas without Li-ion clusters is smaller than areas with Li-ion clusters present. This is most likely the case for all the intermediate phases between graphite and LiC_6.

In addition to the PDF data, the evolution of the 100 graphite peak located at 2.87 $Å^{-1}$ in the *operando* XRD measurement shown in Figure 4.14 in Subsection 4.4.3 could give additional information about the expansion and contraction of the graphite layers themselves. Figure 5.2 shows the different lattice plane classes suggested for the different phases that occur during evolution of the 100 graphite peak.

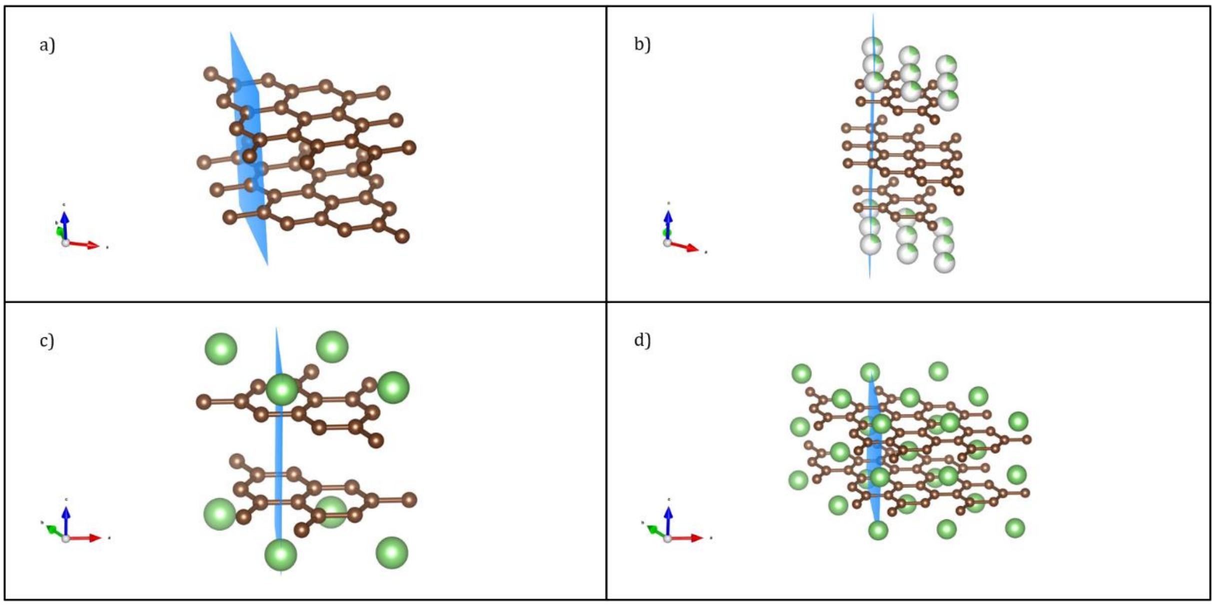

Figure 5.2: Illustration of the different lattice plane classes for different phases of graphite. a) Graphite [100], b) LiC_{30} *[100], c)* LiC_{12} $[\bar{2}10]$ *and* LiC_6 $[\bar{2}10]$*.*

The peak shift during evolution of graphite 100 is significantly smaller than that of graphite 002. The overall peak shift for the 100 graphite peak is 2.87 $Å^{-1}$ (2.14 Å d-spacing) to 2.64 $Å^{-1}$ (2.16 Å d-spacing), while 002 graphite has an overall peak shift from 1.83 $Å^{-1}$ (3.36 Å d-spacing) to 1.67 $Å^{-1}$ (3.69 Å d-spacing). We have seen from the PDF data that the expansion of the hexagonal carbon rings is small. The change in plane position shown for the different LIG phases in Figure 5.2 , could be attributed to the shift of the individual graphene layers from ABAB stacked graphite to AA stacked LiC_6. However, the total shift of the layers is 1.42 Å (measured from the crystal structures of graphite and LiC_6) and this change is significantly larger than the shift we observe for the evolution of the 100 peak. Therefore, the evolution of the 100 graphite peak shows the expansion of the hexagonal carbon rings in the graphene layers showing that graphite does not only expand its interlayer distance but the graphene layers expand. There is a concern with the lattice plane classes Missyul *et* al. proposed for the different phases that occur during evolution of the 100 graphite reflection. The authors propose Miller indices 100 for graphite and LiC_{30} and $\bar{2}10$ for LiC_{12} and LiC_6, which are completely different [38]. The structures Missyul *et al*. propose for LiC_{18} ($P6_3mc$) and LiC_{12} (P6/mmm) have space groups that have no symmetry relation. Therefore, a forbidden phase change must take place and this cannot occur unless a massive amount of energy is put into or taken out of the system, which does not seem to be the case during electrochemical cycling at room temperature. In our *operando* data we do see that these reflections (evolution of 100 graphite) are related, and therefore the structures proposed by Missyul *et* al. are incorrect.

Our PDF and *operando* XRD measurements show that the expansion graphite experiences during lithiation and delitiation is not as simple as initially believed, where it is only the change in interlayer distance and shift of layers. Here we observe see here that the layers themselves contract and expand as the C-C distances in the hexagonal carbon rings change lengths and also the bending of the individual graphene layers that occur due to the insertion of Li-ions as clusters that form “islands”, resembling those described in the Daumas-Herold model. The evolution of the many graphite reflections in our *operando* XRD data shows that the expansion of the material is more complex than initially thought.

Graphite particles consists of domains, where the layers in a domain are mostly aligned depending on the different treatment processes it underwent. These individual domains are aligned throughout the graphite particle to maximize Li-ion diffusion, because as previously mentioned, Li-ion diffusion is several orders of magnitude faster between graphene planes ($\sim 10^{-6}$ cm^2 s^{-1}) than along the grain boundaries ($\sim 10^{-11}$ cm^2 s^{-1}) [54]. Based on the structural considerations described above (shifts of graphene layers in lateral dimensions and expansion of the graphene layers), we theorize that during charge and discharge, these domains become more and more misaligned causing the diffusion of Li-ions through the material to become more difficult. Thus, Li-ions must diffuse a greater length along grain boundaries from one domain to the other as Li-ions can only diffuse into a domain through the edge planes. In addition, the misalignment of layers between different domains could lead to trapping of Li-ions and this could again lead to the irreversible capacity that was observed. This may be the reason for what we observe in the *operando* XRD diffractogram of a graphite electrode taken from a commercial pouch cell that had been cycled around 1100 electrochemical cycles until it reached a retained capacity of ca. 70 % (Figure 4.16 in Subsection 4.4.3). At C/20 (Figure 9.3 in Appendix), the graphite sample is able to transition fully to LiC_6 and back, but not at C/6 as it stops at LiC_{12} despite C/6 still being rather slow cycling. We have seen that C/6 is adequate for pristine and short term cycled samples. However, for the samples which experienced many lithiation and delithiation cycles, aging problem that could be a combination of misalignment of domains that limit diffusion and entrapment Li-ions between domains in the grain boundaries. We most likely did not witness this for our own cycled sample measured at RECX lab at UiO (Figure 4.13 in Subsection 4.42) as graphite tested in this experiment had cycled for a shorter duration compared to the sample taken from the cycled pouch cell. Our cells cycled for 500 cycles, but the capacity disappeared rather quickly and therefore did not go through 500 full electrochemical cycles from graphite to LiC_6 and back. The electrodes from the pouch cell had stable capacities during its whole cycling down to 69% SoH (State of health), which corresponds to approximately 1100 cycles and these cells most likely cycled through many more complete transitions from graphite to LiC_6 and back. The observation to be made here is that with repeated cycling, long term cycling of hundreds or perhaps thousands of cycles will result in the need of lower and lower C-rates in order to allow sufficient time for Li-ions to diffuse and fully lithiate the structure. Essentially, this highlights an important aspect of the degradation mechanism of graphite.

Lithiation and delithiation is by no means a simple mechanism to explain. Intercalation into pure graphite is shown to be thermodynamically driven, but kinetically limited [57], as Li-ions must be forcefully pushed into a structure that maintains its interlayer distance due to the van der Waals forces keeping the graphene layers together. When Li-ion eventually enter between the graphene layers it will essentially get stuck in that position until it is pushed by another Li-ion due to the repulsion that occurs between them. We mentioned previously that individual graphene layers are deformed when clusters of Li-ions are present in graphite. This bending could facilitate easier insertion for Li-ions above and below. The intercalation will be at random and clusters will be distributed randomly throughout the structure and when a threshold is reached, it will undergo a phase transition and overall interlayer expansion occurs. Distribution throughout the structure, even if random, is needed to expand the layers as large areas of unoccupied graphite will prefer the interlayer distance it already has.

The concept of perfectly aligned domains become less reliable when realizing that the measured XRD data is an average of the whole measurement area. Therefore, LiC_{12} will be a phase of lithiated graphite eventually when enough Li-ions are intercalated into the structure, regardless of position of Li-ion clusters in the graphite structure. Transport of Li-ions in the structure happens along the layers. It is not possible for Li-ions to diffuse through the basal plane, through hexagonal carbon rings due to the steric hinderance, adsorption energy and diffusion barrier height. This is true for a defect free structure, but what if there are defects present? Yao *et al*. looked at different defects using DFT calculations in order to see if there were any defects that would allow the diffusion through the basal plane and found that it is possible for Li-ions to diffuse through a carbon ring consisting of 8 carbon atoms as it provides a rather large open space with an adsorption energy -2.36 eV near the two dimers such that a large separation distance of 2.90 Å is maintained [58]. This minimizes the electrostatic charge overlap and maintains a bond length of 1.83 Å that minimizes steric hinderance. They then state that the charge difference between the adsorption and the barrier is 0.04 eV and states that the barrier height ,2.36 eV, can be overcome under typical charging conditions of a battery. However, our group concluded through modelling that Li-ions that try to diffuse through this type of defect will get stuck once it is sitting in the 8-atom ring: there is insufficient energy to push the Li-ion through the defect and into the adjacent interlayer space, where the next graphene sheet would have to be physically pushed away to accommodate the Li-ion.

In our high resolution *operando* data acquired at ESRF (Figure 4.14 in Subsection 4.4.3), we noticed that lithiation and delithiation are different from each other, which is also seen in Figure 2.8 in Section 2.3. Surprisingly, delithiation is not the mirror image of lithiation. We theorize that an important factor here is the starting point and driving force behind the Li-ion transport. For lithiation, we start with a graphite structure that ideally has no Li-ions in the structure and lithiation is thermodynamically driven and kinetically limited. Delithiation starts with LiC_6 where the distance between graphene layers is fully expanded and equal for all layers. Thus, the transport of Li-ions out of the graphite structure is thermodynamically driven and the shifting of layers from AA stacking in LiC_6 to ABAB stacking in graphite, and reduction in interlayer distance between the layers provide additional driving force for transporting Li-ions out of the structure. We examined the diffraction peaks around the Stage 3-2 transition for lithiation and delithiation and these peaks are shown in Figure 5.3.

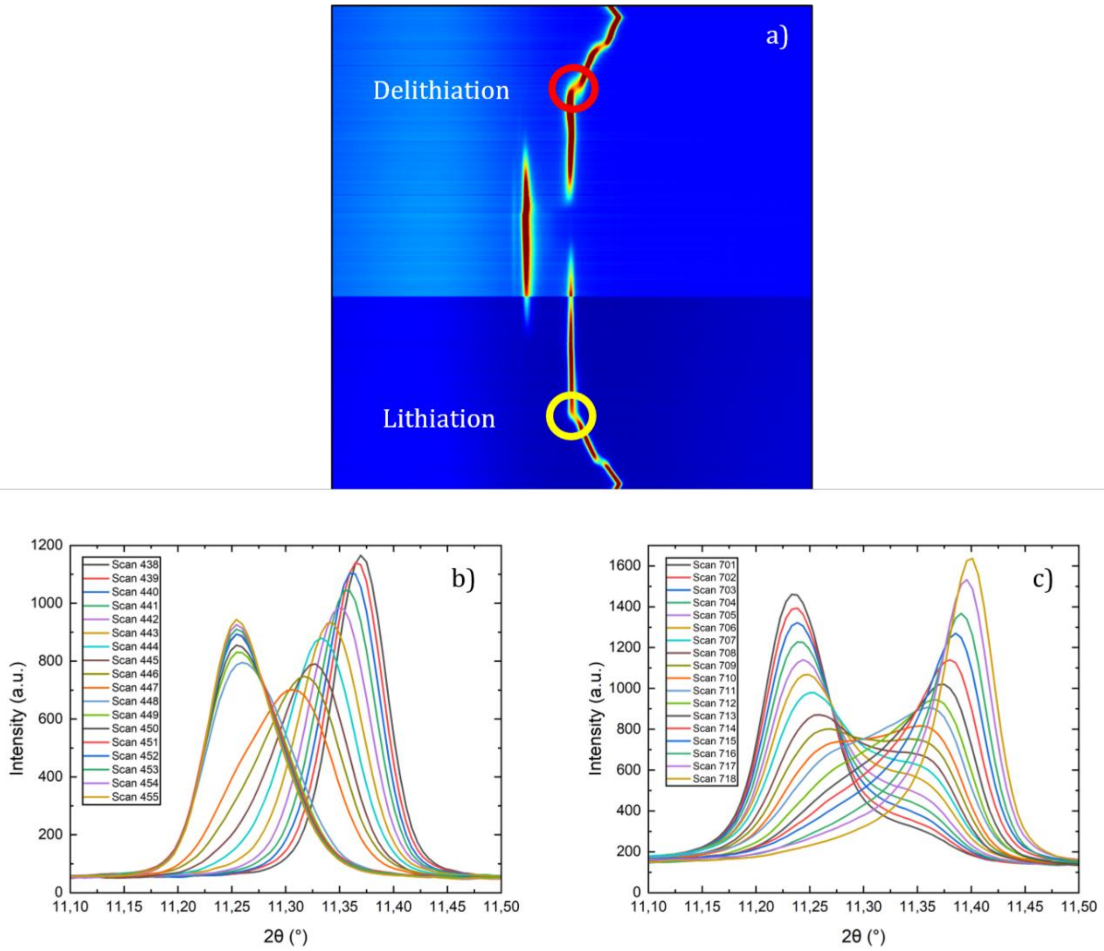

Figure 5.3 Diffraction peaks during lithiation and delithiation for sample G1 from Figure XX in Subsection XXX. a) Yellow circle contains diffraction peaks for lithiation and red circle contains diffraction peaks for delithiation, b) diffraction peaks from the area marked with the yellow circle and c) diffraction peaks from the area marked with the red circle.

These diffraction peaks illustrate that the transitions occurring for lithiation has more of a solid solution type of behavior as we observe the peak shifting in position from scan 438 to 455 (Figure 5.3 b)), while transitions during delithiation behaves as a two-phase reaction, observed from scan 701 to 718 (Figure 5.3 c)), where one diffraction peak has a reduction of intensity, while the other peak has an increase of intensity. Therefore, we speculate that lithiation does not show ordered intermediate phases and the distribution of Li-ions in the graphite structure is mostly random until it reaches Stage 1 of ordered LiC_6. While the observed two-phase transition during delithiation indicate ordered structures where the Li-ions deintercalated in a more organized fashion. We theorize that between ordered end members, graphite and LiC_6, a range of more or less disordered structures occur. These structures have enough overall order at times, over a huge number of graphene sheets, to produce scattering patterns that can be fitted with the unrealistic phases LiC_{30}, LiC_{18} and LiC_{12}. The peak broadening we observe during the "staging" in Figure 5.3 is an indication of this disorder. This type of peak broadening and solid solution and two-phase behavior was also observed by Mathiesen *et al.* [41]. The authors explained that a correlation between the peak broadening and lithiation states indicate that the peak broadening is related to the decrease in coherent in-plane diffraction domain size or to strain broadening due to charge transfer occurring between lithium and the graphene layers. The observation of solid solution behavior and two-phase transition emphasizes the importance of performing *operando* measurements as it is not possible to separate solid solution behavior and two-phase transition with *ex situ* characterization.

6. Conclusions

The primary objective of this study was to understand the electrochemical behavior of graphite and correlate it to the structural changes graphite undergoes during cycling.

Optimizing the electrochemical performance of graphite proved to be more challenging than initially anticipated. We observed multiple challenges during GC, the rather rapid loss of capacity and discrepancies between cells fabricated from the same electrode sheet. We explored different aspects as altering steps in the slurry production, testing different electrolyte compositions with and without FEC and testing different parameters in the GC program as voltage window, 0.01-2.0 V vs Li/Li$^+$ and 0.005-2.0 V vs Li/Li$^+$ and current densities 100 mAh g^{-1} and 50 mAh g^{-1}, yet most of these changes did not significantly improve the electrochemical performance. However, the use of electrolyte with FEC as an additive altered the electrochemical performance resulting in better capacity retention compared to cells that used electrolyte without FEC.

To completely understand the structural changes taking place in graphite during cycling, we analysed the multiple graphite reflections 002, 100, 101, 102 and 004 measured with *operando* XRD. As a result, it became clear that these structural changes are not as simple as described in the literature and are not limited to the changes in interlayer distance and shift of graphene layers from ABAB stacked graphite to AA stacked LiC$_6$. We observed that the three different C-C distances in hexagonal carbon rings (1.41 Å, 2.47 Å and 2.85 Å) changes during lithiation and delithiation, which shows that the graphene layers expand and contract during electrochemical cycling. Therefore, the expansion of graphite occurs in all 3 dimensions.

The evolution of 002 reflection of graphite to 001 reflection corresponding to LiC$_6$ showed that delithiation is not the mirror image of lithiation. A closer observation of the diffraction peaks around Stage 3-2 transition showed that lithiation has solid solution like behavior indicating disordered intermediate phases, while delithiation has two-phase transition indicating ordered structures where Li-ions deintercalate in a more organized manner.

We also utilized *operando* XRD to monitor the structural changes in graphite during lithiation and delithiation at different stages of cycling. Thus, a variety of graphite samples, pristine and cycled, were evaluated with different C-rates and we observed similar behavior for different samples. Thus, the structural changes occurring in graphite are not specific to a particular sample and are essentially generic. Higher C-rates affected the lithiation of graphite as pristine samples were able to fully transition to LiC_6 at C/6 during lithiation, but at C/2 this process stops at LiC_{12}. We also observed that an “ageing” process occurs for graphite that has undergone many hundreds of electrochemical cycles. Specifically, graphite electrodes cut from commercial cycled pouch cells were able to fully transition to LiC_6 during lithiation carried out at C/20, but not at C/6 as it transitioned to LiC_{12}. This “ageing” phenomenon was explained by the occurrence of structure altering processes such as damage to the graphite structure and misalignment of graphite domains that require slower C-rates to give adequate time for Li-ions to lithiate the graphite structure.

7. Future work

In this work, we looked at the electrochemical performance and structural changes in different graphite samples to unravel the lithiation and delithiation mechanisms. Even though we plan to publish this work in the nearest future, several aspects will require additional attention.

During electrochemical performance testing, we have noticed a capacity increase that had not been seen before by Guo *et al.*[52]. Therefore, it would be interesting to assess the origin of such capacity increase further. This could be performed through *operando* XRD in this area of interest to see if any significant change in peak positions or intensity occur: Such study should be combined with the cross-sectional Sem of the electrodes to analyse the changes at the macroscale.

TEM was shown to be an important tool that could aid in explaining the structural change in graphite during lithiation and delithiation. Weng *et al*. did cryo-TEM on graphite samples with different voltages to see how the structure looked, and they could see the individual graphene layers [29]. To further build upon this method is to utilize *operando* TEM to be able to see the movement of the graphene layers as the structure is being lithiated and delithiated.

The experimental data gives valuable information on the structural changes which graphite undergoes during lithiation and delithiation. However, it is difficult to visualize how the different stages between graphite and LiC_6 look like. This is particularly challenging as the structural changes occur in all 3 dimensions and using conventional 2D figures is hard to represent the actual changes in the material. Therefore, computational methods such as modelling is a valuable tool as it is able to visualize the dynamic graphite structure that changes during lithiation and delithiation.

In addition to all of the above, it is clear that substantial chemical transformations take place between the grain boundaries in a graphite particle. Therefore, an analysis of these changes will be of high importance to further understand the mechanism of graphite electrochemical functionality.

8. References

1. Fleischmann, J., M. Hanicke, E. Horetsky, D. Ibrahim, S. Jautelat, M. Linder, P. Schaufuss, L. Torscht, and A.v.d. Rijt, *Battery 2030: Resilient, sustainable, and circular.* 2023.
2. Shaw, S. *Graphite: Natural graphite remains on EU critical raw materials list, for now*. 2020 [cited 2023 29.04]; Available from: https://www.linkedin.com/pulse/graphite-natural-remains-eu-critical-raw-materials-list-sue-shaw/.
3. Jacoby, M., *It's time to get serious about recycling lithium-ion batteries.* 2019.
4. Kurzweil, P., *Gaston Planté and his invention of the lead–acid battery—The genesis of the first practical rechargeable battery.* Journal of Power Sources, 2010. **195**: p. 4424-4434.
5. Liu, B., J.-G. Zhang, and W. Xu, *Advancing Lithium Metal Batteries.* Joule, 2018. **2**(5): p. 833-845.
6. Whittingham, M.S., *Electrical Energy Storage and Intercalation Chemistry.* Science, 1976. **192**(4244): p. 1126-1127.
7. Mizushima, K., P.C. Jones, P.J. Wiseman, and J.B. Goodenough, *LixCoO2 (0<x<-1): A new cathode material for batteries of high energy density.* Materials Research Bulletin, 1980. **15**(6): p. 783-789.
8. Yazami, R. and P. Touzain, *A reversible graphite-lithium negative electrode for electrochemical generators.* Journal of Power Sources, 1983. **9**(3): p. 365-371.
9. Ozawa, K., *Solid State Ionics1994, 69, 212.* Google Scholar There is no corresponding record for this reference.
10. Asenbauer, J., T. Eisenmann, M. Kuenzel, A. Kazzazi, Z. Chen, and D. Bresser, *The success story of graphite as a lithium-ion anode material – fundamentals, remaining challenges, and recent developments including silicon (oxide) composites.* Sustainable Energy & Fuels, 2020. **4**(11): p. 5387-5416.
11. Xing, B., C. Zhang, Y. Cao, G. Huang, Q. Liu, C. Zhang, Z. Chen, G. Yi, L. Chen, and J. Yu, *Preparation of synthetic graphite from bituminous coal as anode materials for high performance lithium-ion batteries.* Fuel Processing Technology, 2018. **172**: p. 162-171.
12. Yan, S. and A.C. Marschilok, *Conversion-Type Electrodes for Rechargeable Lithium Based Batteries: Case Studies of Iron Based Conversion Materials for Lithium-Ion Batteries and Molybdenum Disulfides for Lithium-Sulfur Batteries*, in *Encyclopedia of Energy Storage*, L.F. Cabeza, Editor. 2022, Elsevier: Oxford. p. 36-46.
13. Brennhagen, A., *Synthesis and electrochemical characterization of thin film iron phosphates as cathode material for Li-ion batteries*. 2019.
14. Deng, D., *Li-ion batteries: basics, progress, and challenges.* Energy Science & Engineering, 2015. **3**(5): p. 385-418.
15. Chatterjee, A., *X-ray diffraction.* Handbook of analytical techniques in concrete science and technology, 2000: p. 275-332.
16. Rietveld, H.M., *A profile refinement method for nuclear and magnetic structures.* Journal of Applied Crystallography, 1969. **2**(2): p. 65-71.
17. Coelho, A.A., *TOPAS and TOPAS-Academic: an optimization program integrating computer algebra and crystallographic objects written in C++.* Journal of Applied Crystallography, 2018. **51**(1): p. 210-218.
18. Billinge, S.J., *The atomic pair distribution function: past and present.* Zeitschrift für Kristallographie-Crystalline Materials, 2004. **219**(3): p. 117-121.
19. Fjellvåg, H. *Elektronmikroskop*. 2021 26.04.2023]; Available from: https://snl.no/elektronmikroskop.
20. Jensen, M., *Synthesis and Characterization of Pt1-xPdx Nanoparticles and their Suitability for NH3 Oxidation Catalysis*. 2017.
21. Sottmann, J., R. Homs-Regojo, D.S. Wragg, H. Fjellvåg, S. Margadonna, and H. Emerich, *Versatile electrochemical cell for Li/Na-ion batteries and high-throughput setup for combined*

operando X-ray diffraction and absorption spectroscopy. Journal of Applied Crystallography, 2016. **49**(6): p. 1972-1981.

22. Drozhzhin, O.A., I.V. Tereshchenko, H. Emerich, E.V. Antipov, A.M. Abakumov, and D. Chernyshov, *An electrochemical cell with sapphire windows for operando synchrotron X-ray powder diffraction and spectroscopy studies of high-power and high-voltage electrodes for metal-ion batteries.* Journal of Synchrotron Radiation, 2018. **25**(2): p. 468-472.
23. Rüdorff, W. and U. Hofmann, *Über graphitsalze.* Zeitschrift für anorganische und allgemeine Chemie, 1938. **238**(1): p. 1-50.
24. Daumas, N. and A. Herold, *Relations between phase concept and reaction mechanics in graphite insertion compounds.* Comptes Rendus Hebdomadaires Des Seances De L Academie Des Sciences Serie C, 1969. **268**(5): p. 373-&.
25. Kirczenow, G., *Kinetics of stage ordering and stage transitions.* Physical review letters, 1985. **55**(25): p. 2810.
26. Levi-Setti, R., G. Crow, Y. Wang, N. Parker, R. Mittleman, and D. Hwang, *High-resolution scanning-ion-microprobe study of graphite and its intercalation compounds.* Physical review letters, 1985. **54**(24): p. 2615.
27. Thomas, J.M., G. Millward, R. Schlögl, and H. Boehm, *Direct imaging of a graphite intercalate: evidence of interpenetration of 'stages' in graphite: ferric chloride.* Materials Research Bulletin, 1980. **15**(5): p. 671-676.
28. Dimiev, A.M., G. Ceriotti, N. Behabtu, D. Zakhidov, M. Pasquali, R. Saito, and J.M. Tour, *Direct Real-Time Monitoring of Stage Transitions in Graphite Intercalation Compounds.* ACS Nano, 2013. **7**(3): p. 2773-2780.
29. Weng, S., S. Wu, Z. Liu, G. Yang, X. Liu, X. Zhang, C. Zhang, Q. Liu, Y. Huang, Y. Li, M.N. Ateş, D. Su, L. Gu, H. Li, L. Chen, R. Xiao, Z. Wang, and X. Wang, *Localized-domains staging structure and evolution in lithiated graphite.* Carbon Energy, 2023. **5**(1): p. e224.
30. Menictas, C., M. Skyllas-Kazacos, and T.M. Lim, *Advances in batteries for medium and large-scale energy storage: types and applications*. 2014: Elsevier.
31. Dahn, J., *Phase diagram of Li x C 6.* Physical Review B, 1991. **44**(17): p. 9170.
32. Heß, M. and P. Novák, *Shrinking annuli mechanism and stage-dependent rate capability of thin-layer graphite electrodes for lithium-ion batteries.* Electrochimica Acta, 2013. **106**: p. 149-158.
33. Didier, C., W.K. Pang, Z. Guo, S. Schmid, and V.K. Peterson, *Phase Evolution and Intermittent Disorder in Electrochemically Lithiated Graphite Determined Using in Operando Neutron Diffraction.* Chemistry of Materials, 2020. **32**(6): p. 2518-2531.
34. Billaud, D. and F.X. Henry, *Structural studies of the stage III lithium–graphite intercalation compound.* Solid State Communications, 2002. **124**(8): p. 299-304.
35. Billaud, D. and F. Henry, *Structural studies of the stage III lithium–graphite intercalation compound.* Solid state communications, 2002. **124**(8): p. 299-304.
36. Zheng, T. and J. Dahn, *Effect of turbostratic disorder on the staging phase diagram of lithium-intercalated graphitic carbon hosts.* Physical Review B, 1996. **53**(6): p. 3061.
37. Guerard, D. and A. Herold, *Intercalation of lithium into graphite and other carbons.* Carbon, 1975. **13**(4): p. 337-345.
38. Missyul, A., I. Bolshakov, and R. Shpanchenko, *XRD study of phase transformations in lithiated graphite anodes by Rietveld method.* Powder Diffraction, 2017. **32**(S1): p. S56-S62.
39. Brennhagen, A., C. Cavallo, D.S. Wragg, J. Sottmann, A.Y. Koposov, and H. Fjellvåg, *Understanding the (De)Sodiation Mechanisms in Na-Based Batteries through Operando X-Ray Methods.* Batteries & Supercaps, 2021. **4**(7): p. 1039-1063.
40. Schweidler, S., L. de Biasi, A. Schiele, P. Hartmann, T. Brezesinski, and J. Janek, *Volume Changes of Graphite Anodes Revisited: A Combined Operando X-ray Diffraction and In Situ Pressure Analysis Study.* The Journal of Physical Chemistry C, 2018. **122**(16): p. 8829-8835.

41. Mathiesen, J.K., R.E. Johnsen, A.S. Blennow, and P. Norby, *Understanding the structural changes in lithiated graphite through high-resolution operando powder X-ray diffraction.* Carbon, 2019. **153**: p. 347-354.
42. Cañas, N.A., P. Einsiedel, O.T. Freitag, C. Heim, M. Steinhauer, D.-W. Park, and K.A. Friedrich, *Operando X-ray diffraction during battery cycling at elevated temperatures: A quantitative analysis of lithium-graphite intercalation compounds.* Carbon, 2017. **116**: p. 255-263.
43. Raj, A., I.A. Shkrob, J.S. Okasinski, M.-T. Fonseca Rodrigues, A.C. Chuang, X. Huang, and D.P. Abraham, *Spatially-resolved lithiation dynamics from operando X-ray diffraction and electrochemical modeling of lithium-ion cells.* Journal of Power Sources, 2021. **484**: p. 229247.
44. Senyshyn, A., O. Dolotko, M. Mühlbauer, K. Nikolowski, H. Fuess, and H. Ehrenberg, *Lithium intercalation into graphitic carbons revisited: experimental evidence for twisted bilayer behavior.* Journal of the Electrochemical Society, 2013. **160**(5): p. A3198.
45. Huang, Y.-K., J. Pettersson, and L. Nyholm, *Diffusion-Controlled Lithium Trapping in Graphite Composite Electrodes for Lithium-Ion Batteries.* Advanced Energy and Sustainability Research, 2022. **3**(8): p. 2200042.
46. Sørensen, D.R., M. Heere, A. Smith, C. Schwab, F. Sigel, M.R.V. Jørgensen, V. Baran, A. Schökel, M. Knapp, and H. Ehrenberg, *Methods—Spatially Resolved Diffraction Study of the Uniformity of a Li-Ion Pouch Cell.* Journal of the Electrochemical Society, 2022. **169**(3): p. 030518.
47. Gallagher, K.G., D.W. Dees, A.N. Jansen, D.P. Abraham, and S.-H. Kang, *A volume averaged approach to the numerical modeling of phase-transition intercalation electrodes presented for LixC6.* Journal of The Electrochemical Society, 2012. **159**(12): p. A2029.
48. Skautvedt, C.E., *Syntese og karakterisering av BiFeO3 som anodemateriale i Na-ionebatterier*. 2022.
49. Liu, Q., T. Zhang, C. Bindra, J.E. Fischer, and J.Y. Josefowicz, *Effect of morphology and texture on electrochemical properties of graphite anodes.* Journal of Power Sources, 1997. **68**(2): p. 287-290.
50. Yao, T., N. Ozawa, T. Aikawa, and S. Yoshinaga, *Analysis of layered structures of lithium–graphite intercalation compounds by one-dimensional Rietveld method.* Solid State Ionics, 2004. **175**(1): p. 199-202.
51. Petkov, V., R. Difrancesco, S. Billinge, M. Acharya, and H. Foley, *Local Structure of Nanoporous Carbons.* Philosophical Magazine B-physics of Condensed Matter Statistical Mechanics Electronic Optical and Magnetic Properties - PHIL MAG B, 1999. **79**: p. 1519-1530.
52. Guo, J., Y. Li, J. Meng, K. Pedersen, L. Gurevich, and D.-I. Stroe, *Understanding the mechanism of capacity increase during early cycling of commercial NMC/graphite lithium-ion batteries.* Journal of Energy Chemistry, 2022. **74**: p. 34-44.
53. Etacheri, V., O. Haik, Y. Goffer, G.A. Roberts, I.C. Stefan, R. Fasching, and D. Aurbach, *Effect of Fluoroethylene Carbonate (FEC) on the Performance and Surface Chemistry of Si-Nanowire Li-Ion Battery Anodes.* Langmuir, 2012. **28**(1): p. 965-976.
54. Persson, K., V.A. Sethuraman, L.J. Hardwick, Y. Hinuma, Y.S. Meng, A. van der Ven, V. Srinivasan, R. Kostecki, and G. Ceder, *Lithium Diffusion in Graphitic Carbon.* The Journal of Physical Chemistry Letters, 2010. **1**(8): p. 1176-1180.
55. Sun, C., X. Ji, S. Weng, R. Li, X. Huang, C. Zhu, X. Xiao, T. Deng, L. Fan, L. Chen, X. Wang, C. Wang, and X. Fan, *50C Fast-Charge Li-Ion Batteries using a Graphite Anode.* Advanced Materials, 2022. **34**(43): p. 2206020.
56. Finegan, D.P., A. Quinn, D.S. Wragg, A.M. Colclasure, X. Lu, C. Tan, T.M.M. Heenan, R. Jervis, D.J.L. Brett, S. Das, T. Gao, D.A. Cogswell, M.Z. Bazant, M. Di Michiel, S. Checchia, P.R. Shearing, and K. Smith, *Spatial dynamics of lithiation and lithium plating during high-rate operation of graphite electrodes.* Energy & Environmental Science, 2020. **13**(8): p. 2570-2584.
57. Bardhan, K.K. and D.D.L. Chung, *A kinetic model of the first intercalation of graphite.* Carbon, 1980. **18**(5): p. 303-311.

58. Yao, F., F. Güneş, H.Q. Ta, S.M. Lee, S.J. Chae, K.Y. Sheem, C.S. Cojocaru, S.S. Xie, and Y.H. Lee, *Diffusion Mechanism of Lithium Ion through Basal Plane of Layered Graphene.* Journal of the American Chemical Society, 2012. **134**(20): p. 8646-8654.

9. Appendix

9.1 Electrochemical measurements

Figure 9.1 is the GC measurements for cells AT_T29_127, AT_T29_128 and AT_T29_129 fabricated from electrode sheet AT_29, that were cycled at voltage window 0.01-2.0 V vs Li/Li$^+$ to compare with cells AT_T29_130, AT_T29_131 and AT_T29_132 that were cycled at voltage window 0.005-2.0 V vs Li/Li$^+$.

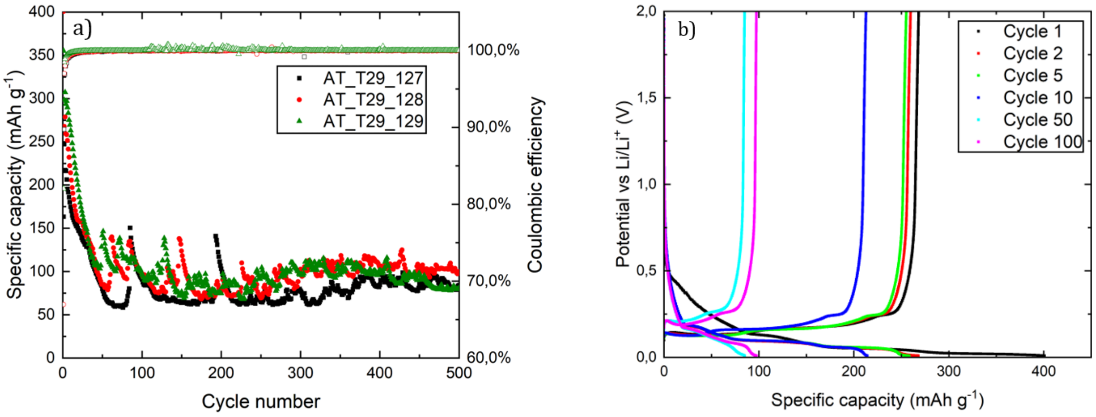

Figure 9.1: a) comparison of GC measurements for cells AT_T29_127, AT_T29_128 and AT_T29_129 displaying the change in specific capacity against cycle number and coulombic efficiency is displayed at the top of the figure. b) shows a representative GC plot for cell AT_T29_128. Electrolyte E2 was used in cell fabrication and voltage window 0.01-2.0 V vs Li/Li$^+$ was used for the GC measurements.

Figure 9.2 shows GC measurements for the second cycling of AT_T17_67 after electrolyte E2 and new Li metal foil was added. Cycled at 100 mAh g^{-1} at voltage window 0.01-2.0 V vs Li/Li$^+$.

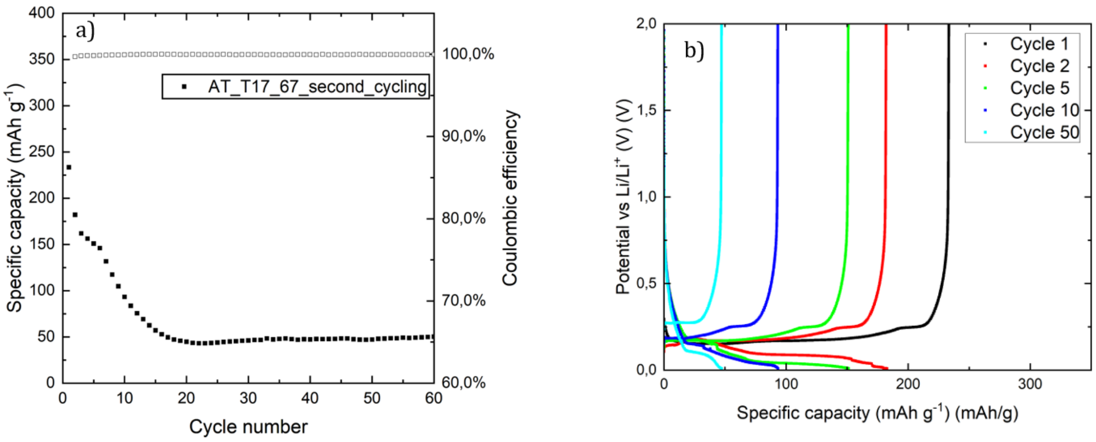

Figure 9.2 GC measurements for AT_T17_67 during second cycling after electrolyte E2 and new Li metal foil was added.

9.2 *Operando XRD*

Figure 9.3 is the *operando* measurement of the cycled pouch cell at C/20 For comparison with the *operando* measurement of the cycled pouch cell at C/6.

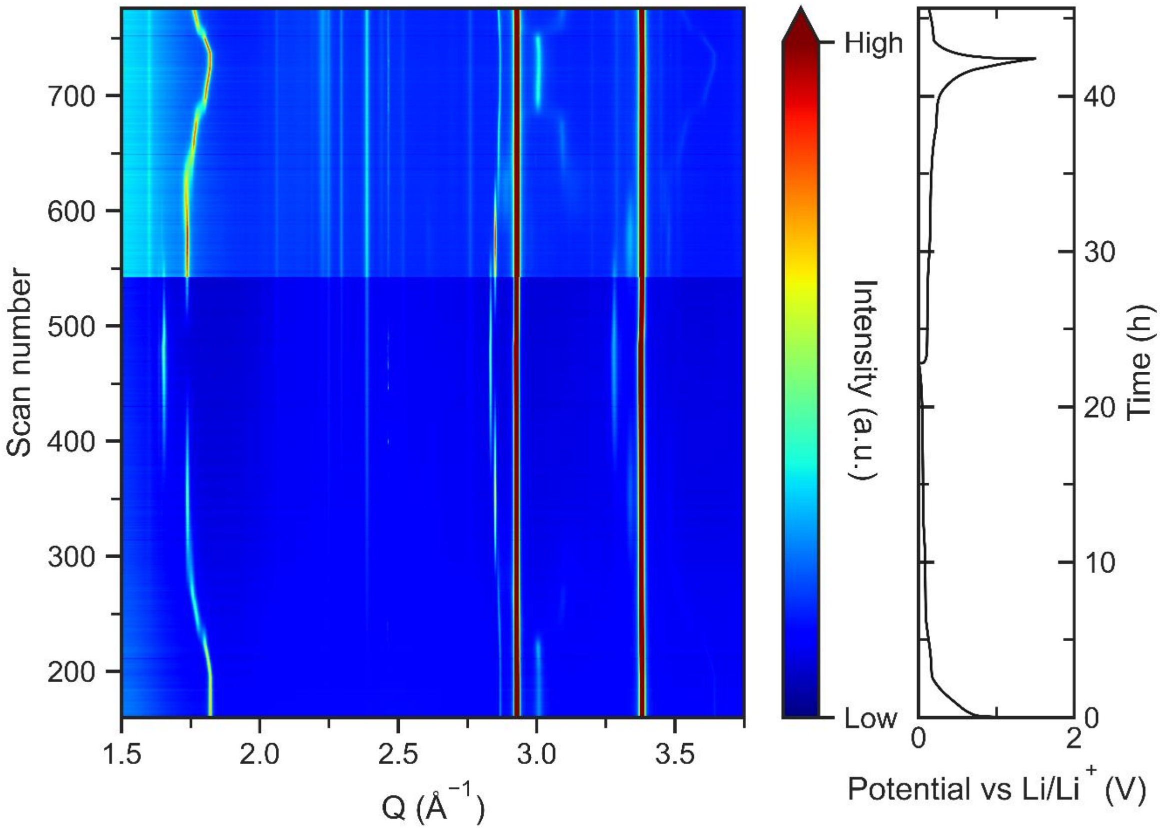

Figure 9.3: The evolution of 002 (1.83 Å^{-1}), 100 (2.87 Å^{-1}), 101 (3.01 Å^{-1}), 102 (3.34 Å^{-1}) and 004 (3.64 Å^{-1}) reflections of graphite from cycled pouch cell (1100 cycles) during galvanostatic cycling with a rate of C/20 (electrochemistry is shown on the right panel of the figure).